



Article

# Power Density Distribution for Laser Additive Manufacturing (SLM): Potential, Fundamentals and Advanced Applications

Alexander S. Metel , Michael M. Stebulyanin, Sergey V. Fedorov and Anna A. Okunkova \*

Department of High-efficiency Machining Technologies, Moscow State University of Technology STANKIN, Vadkovskiy per. 3A, 127055 Moscow, Russia; a.metel@stankin.ru (A.S.M.); m.stebulyanin@stankin.ru (M.M.S.); sv.fedorov@icloud.com (S.V.F.)

\* Correspondence: a.okunkova@stankin.ru; Tel.: +7-909-913-12-07

Received: 9 November 2018; Accepted: 7 December 2018; Published: 30 December 2018



**Abstract:** Problems with the laser additive manufacturing of metal parts related to its low efficiency are known to hamper its development and application. The method of selective laser melting of metallic powders can be improved by the installation of an additional laser beam modulator. This allows one to control the power density distribution optically in the laser beam, which can influence the character of heat and mass transfer in a molten pool during processing. The modulator contributes alternative modes of laser beam: Gaussian, flat top (top hat), and donut (bagel). The study of its influence includes a mathematical description and theoretical characterization of the modes, high-speed video monitoring and optical diagnostics, characterization of processing and the physical phenomena of selective laser melting, geometric characterization of single tracks, optical microscopy, and a discussion of the obtained dependences of the main selective laser melting (SLM) parameters and the field of its optimization. The single tracks were produced using the advanced technique of porosity lowering. The parameters of the obtained samples are presented in the form of 3D graphs. The further outlook and advanced applications are discussed.

**Keywords:** selective laser melting; laser modulation; single track; video monitoring; physical phenomena; Gauss; flat top; top hat; bagel; doughnut

## 1. Introduction

Laser additive manufacturing is a technological method for the direct production or growing of functional objects from powders. Recent research [1–4] has aimed to create new classes of materials as gradient construction and functional materials (with gradient properties for different functional elements of geometrically complex parts), gradient reinforced by ceramics [5], variations of content for intermetallic alloys, adaptations of the method for hard-to-melt materials as hard alloys based on tungsten or tungsten itself, etc. [6–13].

However, the problem of its efficiency remains unsolved [14–19], and the application of the method in each case requires significant energy and finances, which hampers the development of this production technique and its applications. Today, common conventional selective laser melting (SLM) or selective laser sintering (SLS) machines allow for producing parts with a maximum laser power of about 400 W [20–22]. Some manufacturers create machine tools with an available power of about 1 kW [23,24]. Hence, more than 96% of the work is done with a maximum laser power in the range of 30–100 W to provide higher quality and resolution of the produced objects [25,26].

The problem is related to the impossibility of directly increasing the laser power without a decrease in the quality of the manufactured objects [27–30]. The direct augmentation of the main

SLM parameters leads to an unpredictable and dramatic decrease of the product quality, which is traditionally associated with an excess of energy in the molten pool.

The quality of the object produced by SLM is defined by the geometrical accuracy of the operational surfaces of the product and its mechanical properties. The geometrical accuracy depends, in turn, on the geometrical accuracy of the deposited layers and the volumetric accuracy of the 3D model, thickness of layers, and maximum average particle size (Figure 1). The primary interest of the current paper is in the influence of the main SLM parameters and the maximum values achieved by the redistribution of the energy in the laser beam on the main characteristics of the deposited tracks (marked in red in Figure 1). Another aspect of the achieved research results is the reduction of the molten pool depth with changes of the laser beam profile, which influence the previous layers and substrate material by a remelting process, which influences the chemical homogeneity of the produced object and reduces the thickness of the intermediate space between the substrate and the object. Usually, this intermediate space is cut out during consequent post-treatment of the object. Its reduction will have a positive influence on the reduction of the object's costs, including auxiliary timing and material losses during post-processing (marked in purple in Figure 1).

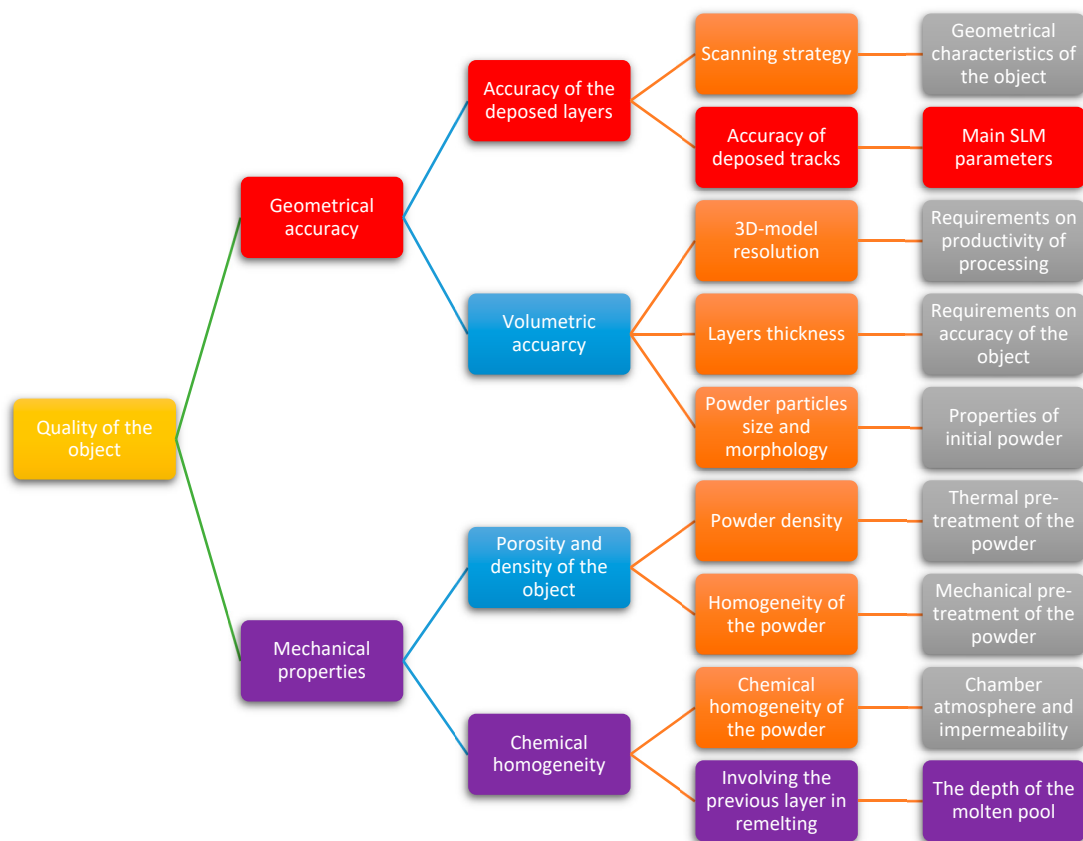


**Figure 1.** Graphical representation of the main technological aspects of selective laser melting /sintering, parameters and conditions and their influence on the quality of the object.

It should be noted that there are several known ways to improve the quality of the parts produced by selective laser melting based on the results of experimental investigations [31–35]:

- An initial analysis of the control factors related to SLM machines on the prepared powders before production with the purpose of receiving confirmed experimental data of the current conditions of the materials and environment;
- Improved techniques for pre-treatment of the powders: mechanical pre-treatment with the purpose of obtaining more regular shapes and sizes in the initial powder; thermal pre-treatment

of the powders with the intent to remove excess air in powder and increase the density of the powder;

- Improved techniques in mechanical post-treatment of the produced objects with the purpose of obtaining smoother surfaces; thermal post-treatment of the object with the intention of improving the internal microstructure and mechanical properties of the produced object;
- Installation of in situ optical monitoring tools with the aim to control processing.

Meanwhile, all of them are related to the increase in production time as well. Hence, the purpose of the current study is to develop and investigate a technique to increase the productivity of SLM processing with no losses in the quality of the produced object. The main tasks of the study were formulated as follows:

- (1) Investigation of principal abilities of laser power redistribution at the spot and mathematical corroboration of the developed approach;
- (2) Development of the experimental setup for power density redistribution and verification of the developed system;
- (3) Demonstration of energy redistribution using the designed system and characterization of the specimens;
- (4) Supporting the obtained data by video monitoring and optical diagnostics.

## 2. Materials and Methods

### 2.1. Experimental Setup

The experiments were carried out on an experimental setup developed by Moscow State Technological University (MSTU) Stankin [36,37].

The optical part of the setup consists of laser beam shaping and optical monitoring systems. An ytterbium fiber optic laser LK-200-V3 (IRE-Polus, Fryazino, Moscow, Russia) with maximum power 200 W (maximum available power in output was less than 173 W) and wavelength  $\lambda = 1.07 \mu\text{m}$  was used. The laser source with maximum power of 200 W was chosen for safety reasons as it was supposed to work well with the open system of the machine [38,39]. The industrial SLM machine does not provide access to the working chamber and full access to system parameters, or its access is limited [40,41].

A 5-mm diameter collimated laser beam passes through a Focal-piShaper ( $\pi$ Shaper, Berlin, Germany), gets into a scanning head and deviates according to the signal from a scanning program from a PC by a system of reflective mirrors. Further it passes through an focal ( $f$ -Theta) lens [42,43] and impacts the powder layer on a substrate made in the form of a disc. A charge-coupled device (CCD) camera LaserCam-HR (Coherent, Palo Alto, CA, USA) controls power distribution in a laser beam. An optic mirror B-Cube and attenuator C-Varm (Coherent, Santa Clara, CA, USA) were used for laser beam power reducing on the surface of the camera matrix. A high-speed camera FastcamSA5 (Photron, San Diego, CA, USA) and macro object-glass Zoom6000 (Navitar, New York, NY, USA) were used for processing visualization and monitoring. The laser diode lighting Cavilux HF (Cavitar, Tampere, Finland) with 810 nm filter was used to exclude the influence of laser and thermal radiation in the working zone. The parameters of the shooting were chosen for optimal detection of the powder outburst from the processing area: frame rate and lighting pulses rate 1000 Hz, resolution  $1024 \times 1024$ , shutter time 999  $\mu\text{s}$ .

The mechanical part of the setup consists of a working table with two moving pistons: one for raw powder, another one for building an object. The motions of the pistons in cylinders were controlled using a metric rule. The objects and single tracks were produced on replaceable 10 mm height and 50 mm diameter discs made of constructional carbon steel 1020 by AISI (Standards of The American Iron and Steel Institute). A built-in metallic equalizer rod realized deposition of the powder

automatically. An application developed for a computer synchronized the movements of the built mechanisms [44,45].

## 2.2. Methods for Converting the Mode Composition of Laser Radiation

Laser radiation is generated using special optics, which has a different configuration. All optics obey the laws of diffraction, which are the basis for the description of various optical effects.

A theoretical description of optical effects usually begins with the so-called Fresnel-Kirchhoff diffraction formulas. However, these equations are usually quite complex and not practical for technical purposes, and, therefore, they use various simplifications such as the Fresnel and Fraunhofer approximations.

The well-known and widely used conclusion of the theory of diffraction is as follows: the amplitude of the light distribution field in a particular case, in the focal plane of the lens, is proportional to the Fourier transform of the input amplitude of the field distribution.

An example of these transformations is shown in Figure 2. This figure shows the results for the attractive cases for practical purposes:

- (a) focusing a TEM<sub>00</sub> (Gaussian) laser beam [46];
- (b) focusing the beam with a “flat top” or “top hat”, TFT (TEM “flat top”) = TEM<sub>00</sub> + TEM<sub>01</sub><sup>\*</sup>, where TFT is TEM “Flat top”, TEM<sub>01</sub><sup>\*</sup> = TEM<sub>01</sub> + TEM<sub>10</sub> [47] (Figure 2a);
- (c) creating a “flat top” beam in the lens focus area, which is one of the most actual optical research topics [48,49].

It is known that when a beam propagates in space due to interference, the distribution density varies in different planes along the propagation path of the laser radiation. In other words, in each plane of the lens, the intensity profile differs from each following profile, in particular, this depends on the initial distribution of the beam intensity profile at the lens input. For example, Figure 2b corresponds to the TEM<sub>00</sub> (Gaussian) plane of the power distribution plane as one of the most common in laser technology. This power distribution density describes the initial distribution in polar coordinates according to the following formula:

$$I_{in}(r) = I_{in0} \exp\left(-\frac{2r^2}{\omega^2}\right), \quad (1)$$

where  $I_{in}$  is the intensity at the entrance of the lens;  $\omega$  is the radius of the Gaussian beam waist; and  $I_{in0}$  is a constant.

The focusing of such a beam leads to the creation of a spot in the focal plane, also with a Gaussian power density distribution and diameter  $d$ , determined according to the following formula:

$$d = \frac{4\lambda f M^2}{2\pi\omega}, \quad (2)$$

where  $\lambda$  is the wavelength, m;  $f$  is the focal length of the lens, m; and  $M^2$  is the quality factor of laser radiation, for TEM<sub>00</sub> Gauss mode  $M^2 = 1$ .

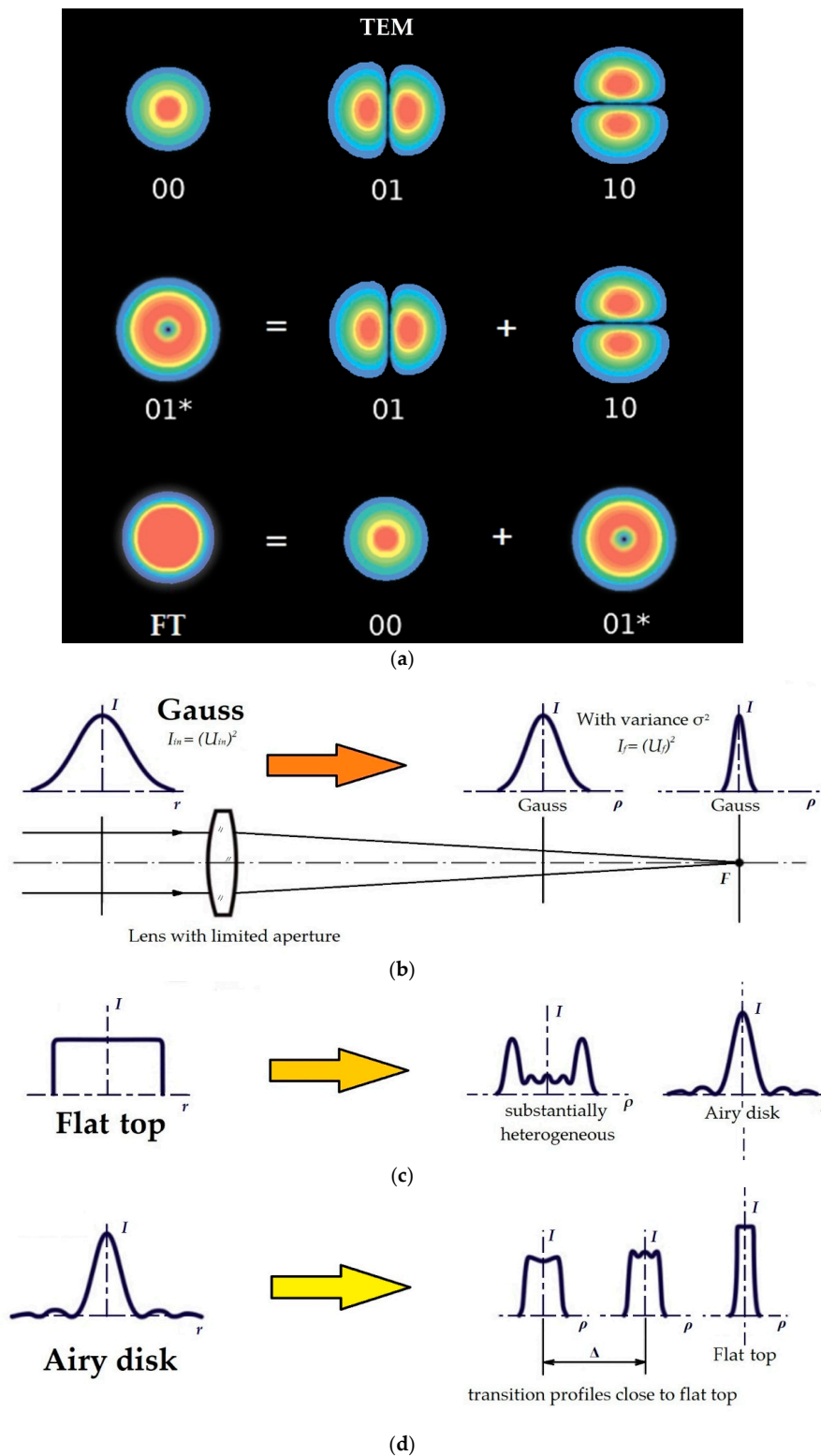


**Figure 2.** The change in the intensity of the radiation profile depending on the characteristics of an input laser beam: (a) simplified presentation of laser beam mode in plane; (b) Gaussian beam; (c) flat-top or top-hat beam; (d) Airy disk;  $I_{in}$  is intensity of input beam,  $W \cdot m^{-2}$ ;  $I_f$  is intensity of focused beam,  $W \cdot m^{-2}$ ;  $U_{in}$  is the complex amplitude of the electric field for input beam, V;  $U_f$  is the complex amplitude of the electric field for focused beam, V;  $r$  is an effective radius of input beam,  $\mu m$ ;  $\rho$  is an effective radius of focused beam,  $\mu m$ ;  $\sigma^2$  is the variance or measure of the spread of random values, non-dimensional;  $F$  is focus, optical point of the system;  $\Delta$  is the distance between intermediate planes.

An essential feature of focusing a beam with a Gaussian distribution of power density is that its intensity profile remains unchanged (Gaussian) throughout the beam propagation; only its geometric characteristics change. This feature of a beam with a Gaussian power density distribution is widely used in laser technology and its various applications. However, for all other profiles, the intensity of distribution varies. For example, in Figure 2c an initial beam with a flat top, characterized by an initially uniform distribution of power density in the focal plane of the focusing lens, is determined by the function called Airy disk, described by the following equation:

$$I_f(\rho) = I_{f0}[J_1(2\pi\rho)/(\pi\rho)]^2, \quad (3)$$

where  $J_1$  is the Bessel function of the first kind and the first order, and  $I_{f0}$  is a constant.

At the same time, in the space between the lens and the focal plane, the interference pattern is different from the initial distribution as a uniform distribution with a flat top and a distribution in the focal plane of the lens. These intermediate distributions are inherently nonuniform and useless for practical applications. Thus, it can be concluded that beam focusing with a flat top in the focal and intermediate planes does not create a spot with a uniform distribution of power density. It makes no sense to focus laser radiation with a uniform distribution of power density in its spot. However, this does not mean that it is impossible to create a spot of laser radiation with a uniform intensity. For example, Figure 2d shows an example of an essential practical task: the creation of a small laser spot with a uniform radiation intensity in the focal plane of the lens.

It is necessary to solve the inverse problem of finding the required power density of laser radiation at the entrance to the focusing lens to obtain the power density distribution with a flat top in the focal plane of the lens to create such a small spot with uniform intensity. For example, attempts to solve this problem were made in [50]. Mathematical calculations based on inverse Fourier transforms were performed. The solution to this problem was the following remarkable conclusion: in order to obtain the uniform distribution of laser radiation in the focal plane, the input beam should have a distribution similar to the Airy disk distribution density described by the Airy function presented above. In other words, to obtain a laser spot with a flat top in the focal plane, the input beam must have a substantially nonuniform profile.

As in the previous cases, the interference pattern in the space between the lens and the focal plane is not constant; it varies in size and intensity of radiation. The intensity distribution with a flat top is only a particular case of a continuous change in the intensity of the distribution. A primary feature of focusing the beam with the Airy disk distribution in creating a beam with a flat top and a near-flat top profile distribution is in possibility not only focusing in the focal plane but also in some intermediate planes. The intermediate planes are labeled  $\Delta$  in Figure 2d. A continuous transition from one intensity profile to another can be seen in the picture.

The presence of this delta range is quite significant from a practical point of view since a profile with a flat top is relatively stable and can be within the tolerance of  $\pm 10\%$ . The change in the diameter of the input beam is not significant, with a change of less than 30%. The spot size is only 1.3–1.7 times larger than the spot in the focal plane; there is a significant depth of field. Thus, it is possible to obtain various power density distributions using a laser beam with the Airy disk distribution and a focusing lens in its focal plane and nearby planes. The most interesting of them for the work are presented in Figure 3.

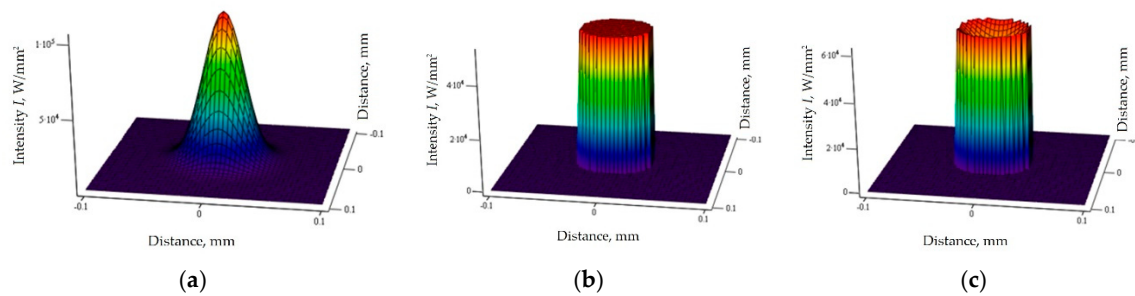


**Figure 3.** The power density distribution of laser radiation in different planes, near the focal plane of the lens: (a) Gauss; (b) flat top; (c) donut.

When studying the influence of the dependences of the mode composition of laser radiation, a laser source with a Gaussian power density distribution and an optical system were used, which converted the Gaussian power density distribution into the Airy disk distribution, which was later focused by a scanning lens.

### 2.3. Achievability of Laser Modes

The camera for measuring the power density of the laser radiation and the geometric characteristics of the laser beam was additionally equipped with two attenuators, B-Cube and C-Varm (Coherent, Santa Clara, CA, USA), with fixed and variable attenuation coefficients, respectively, to enable measurements on a laser operating at minimum power at its focused spot. The B-Cube attenuator reflects up to 5% of the laser power to the perpendicular direction and directs it through a special spacer to the C-Varm attenuator, which directs it to the camera matrix. The camera is located on a tripod that was raised relative to the substrate by an amount equal to the “shoulder” between the center of the first attenuator and the matrix, thus allowing for measuring the geometric characteristics of laser radiation falling directly on the substrate.

The diameter of the output laser radiation from the collimator was 5 mm, and the increasing capacity of the transducer modal composition of the laser radiation was set at two crates. The focus of the laser radiation was found on the substrate (Figure 4a) with a Gaussian power density distribution. The effective diameter of the laser spot was in the range 100–120  $\mu\text{m}$ , and the effective area was 0.309  $\text{mm}^2$ .

Furthermore, with the reverse defocusing relative to the focal plane, a power density was achieved using a converter of the mode composition of laser radiation according to the physical phenomena described above, bringing its characteristics closer to a flat-top density as it presented in Figure 4b. At the same time, the effective diameter of the laser beam was in the range 200–255  $\mu\text{m}$ , and its effective area was 0.447  $\text{mm}^2$ . With an ever-increasing defocusing, the inverse Gaussian or “donut” (doughnut) [51] power distribution density was achieved (Figure 4c). At the same time, the effective diameter of the laser beam was in the range 300–377  $\mu\text{m}$ , and its effective area was 0.379  $\text{mm}^2$ .

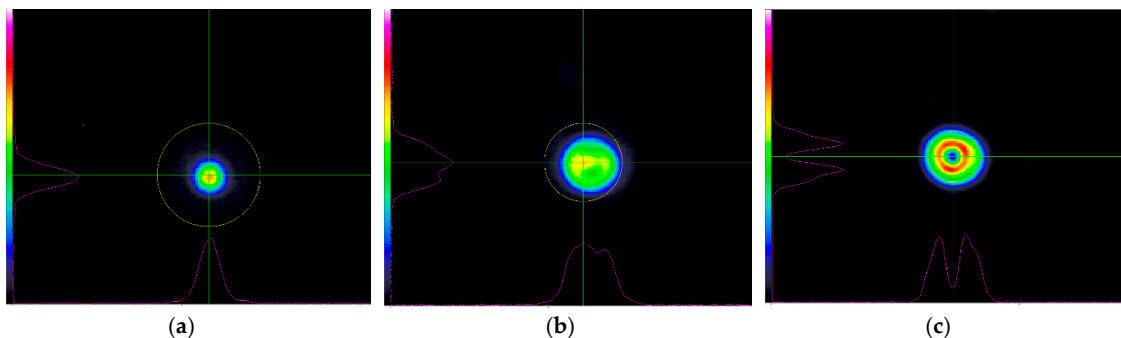


**Figure 4.** The data from a charge-coupled device (CCD) camera with the obtained laser beam profiles: (a) Gauss; (b) flat top (top hat); (c) donut (bagel).

#### 2.4. Powder Material

CoCrMo powder (60–65% of Co, 26–30% of Cr, 5–7% of Mo) was chosen due to its excellent melting properties, heat resistivity, neutral reaction to the protective environment, and wide range of possible industrial applications [52–54]. The granular and morphometric analyses showed that the granules have a mostly spherical shape, which is preferable for better energy absorption [55–57]. The initial CoCrMo powder was sifted using an analytical sieving machine AS200 basic (Retsch, Dusseldorf, Germany) with a test sieve (50  $\mu\text{m}$  by ISO 3310-1) and dried using a vacuum oven VO400 (Mettler GmbH + Co. KG, Schwabach, Germany) before processing. The drying of the powder contributes a better density of the powder in the layers and removes the excess of air. The powder was controlled using an optical particle shape analyzer 500NANO (Occhio, Liege, Belgium) and a scanning electron microscope VEGA 3 LMH 1000000x (Tescan, Brno, Czech Republic). The thickness of the layers during the experiments was controlled optically using Olympus BX51M (RYF AG, Grenchen, Switzerland) and was measured in the range  $79.5 \pm 4.5 \mu\text{m}$ .

#### 2.5. Characterization of the Samples

The characterization of produced samples was provided by an SEM VEGA 3 LMH and by an optical microscope Olympus BX51M. Probe preparation was made using a standard ATM Machine Tools sampling equipment (ATM Machine Tools Ltd., Wokingham, UK). Cross sections of the samples were etched by a mixture of hydrochloric acid HCl (38% solution) and hydrogen peroxide  $\text{H}_2\text{O}_2$  (3% solution) in the proportion 6:1 [58–60].

### 3. Results

#### 3.1. Investigation of Principal Abilities of Laser Power Redistribution in the Spot and Mathematical Corroboration of the Developed Approach

##### 3.1.1. Classification of the Main SLM Parameters and the Way of Laser Power Redistribution

The quality parameters of the deposited single tracks depend on using processing factors, which can be controlled by a numerical control system of the machine. The factors related to SLM machine can be called entirely controlled factors, while the factors associated to the properties of using powder, characteristics of the environment, and even to the quality of initial 3D model presentation can be called partially controlled factors (Figure 5).

There are several possibilities for improving the efficiency of selective laser melting with no loss in quality of the produced object during energy transformation from the laser source to the absorption of the energy during formation of the molten pool, mentioned in Table 1 [61,62]. The described possibilities have no visible effect on the improvement of process efficiency [63–65], except the last one, which can theoretically improve the efficiency by more than 2-3 times [66–68].

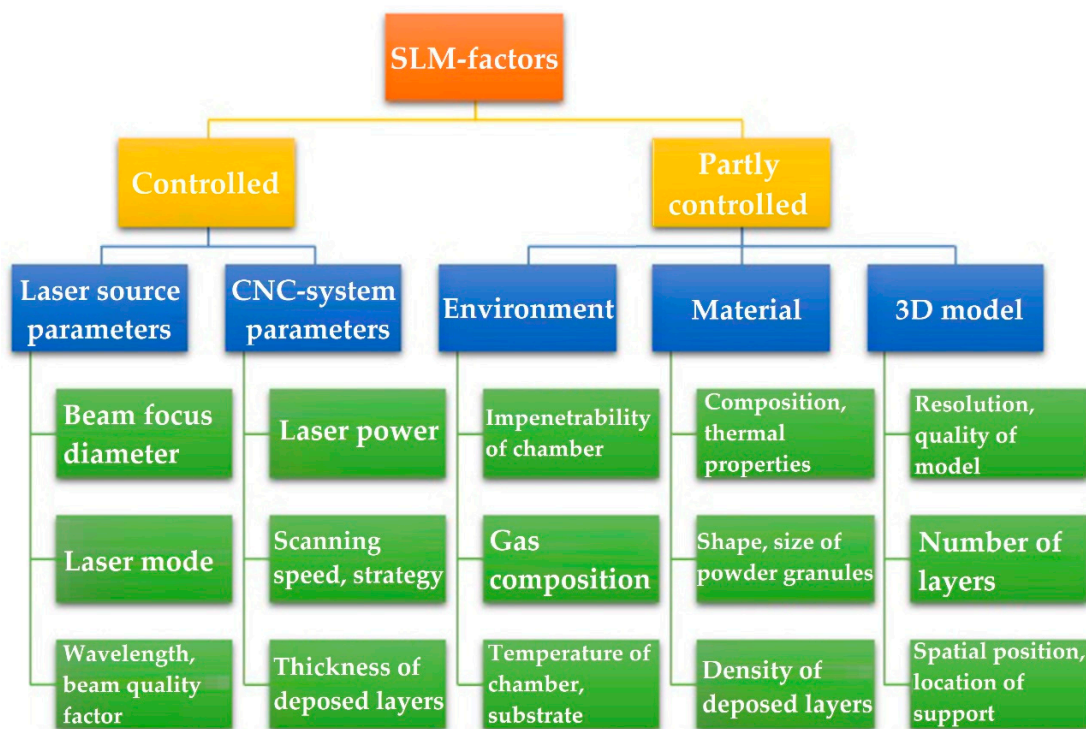


Figure 5. Classification of main SLM factors.

Table 1. The way of energy transformation from the laser source to the molten pool for selective laser melting/sintering.

The Way of Laser Energy Transformation	Optimization on the Way to Reduce the Energy Loss	Theoretical Level of Influence on SLM Efficiency	Practical Level of Influence on SLM Efficiency
1: Laser source	Optimization of wavelength $\lambda$ [3,69]	~0.3–1%	~0.5%
2: Optic system	Brightness enhancement of optic glasses [70]	~1–2%	~0.5%
3: Powder absorption	Coatings, structure of powder surface, pre-heating to reduce a temperature gradient, pre-drying to reduce porosity [71–73]	~10%	~10–15%
4: Heat and mass transfer in a molten pool	Optimization of laser power density distribution	~2–3 times	The subject of study

### 3.1.2. Short Description of the Developed Approach

The knife-like formation of the molten pool, which is not as desirable for other technological laser applications as the precise laser cutting of thick sheets (with thickness more than 5 mm), laser scribing, and graving provoke multiple remelting of the material in the molten pool and interdiffusion with the previous layers due to its excess of energy on the treated surface. The excess of energy is related to the normal bell formed Gaussian distribution. This leads to the formation of a solid solution between the material of the substrate and has effects on the chemical and microstructural homogeneity of the subsequent layers of the object [74]. This effect is related to the character of the energy distribution in the laser spot, which is close to the Gaussian profile and can be approximated by a Gaussian function [18,75].

As the convectional mechanisms of powder consolidation during selective laser melting are thermo-activated, there is a reason for obtaining a uniform temperature field  $T$  induced by the irradiation. It is known that if the thermal energy is released on an adiabatic plane bounding a uniform conducting half-space inside a circle of radius  $r_0$ , with radial distribution, the steady temperature rise over this circle is uniform [76,77]:

$$T_0 = \frac{P}{4k \cdot r_0} [K], \quad (4)$$

where  $P$  is laser power, W; and  $k$  is the thermal conductivity of powder,  $W \cdot (m \cdot K)^{-1}$ .

The beam with the radial distribution as flat top is preferable for more uniform energy absorption and melting of the powder in the laser spot due to the principal mechanism of heat transfer related to the thermal conductivity of the material surface [78,79].

The flat-top profile is available mathematically, but it is almost unachievable on the experimental setup due to the issues described above.

The compromise can be found in Airy distribution of the first harmonic  $TEM_{01}^*$  ( $TEM_{01} + TEM_{10}$ ), which is traditionally called a “bagel,” “donut” or inverse Gaussian profile [80]. Meanwhile, there are more opportunities for direct augmentation of the energetic impact and the possibility of keeping the regular character of the distribution for the inverse Gaussian profile.

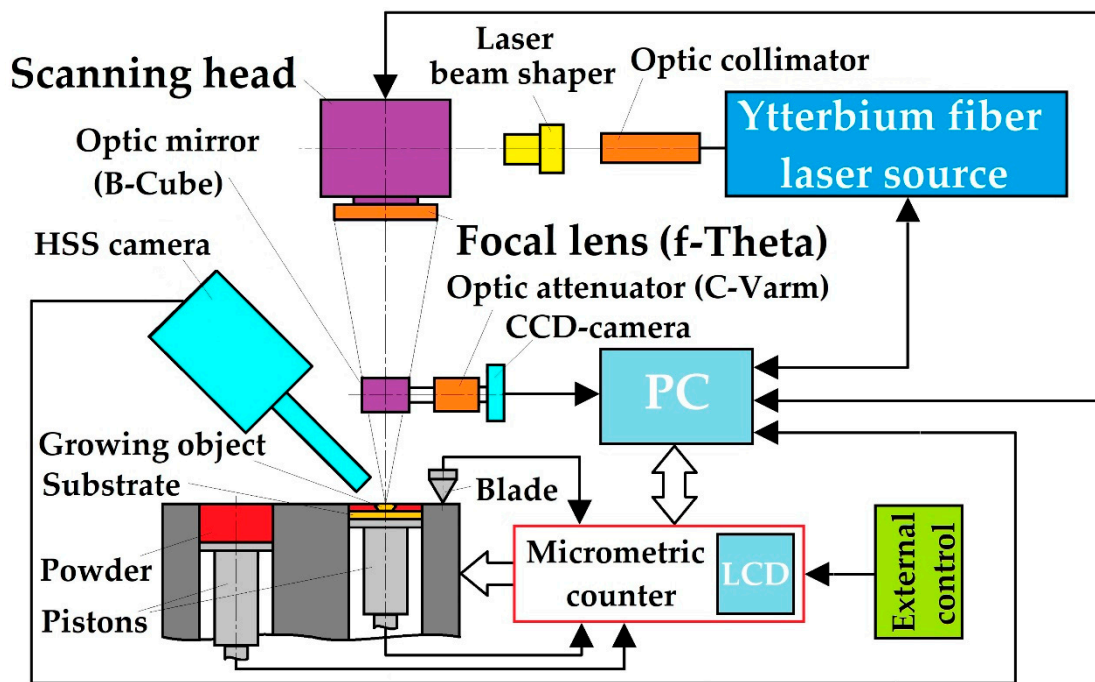
As was previewed, both of the alternative profiles have an absence of the energy peak in the center of the laser beam spot. This can result in a decrease of the intensity of powder granule emission, evaporation of the material from the molten pool, and reduction of low-temperature plasma cloud volumes. That should, in turn, have a positive influence on the quality of production.

### *3.2. Development of the Experimental Setup for Power Density Redistribution and its Approbation*

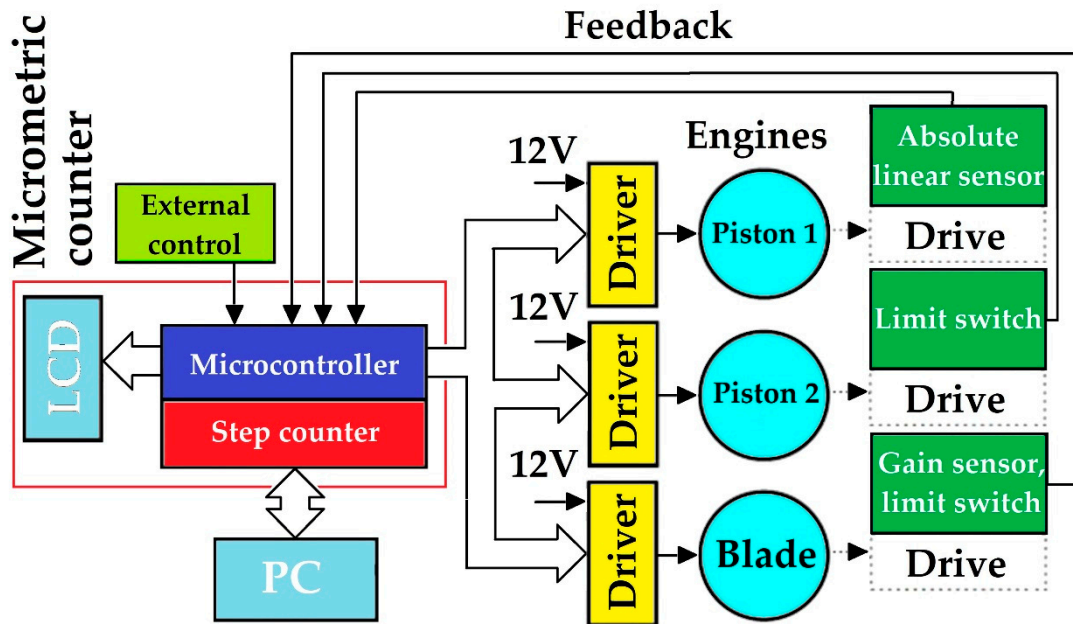
#### *3.2.1. Construction of the Experimental Setup and Laser Beam Modes*

Up until now, the modern mechanical industry has concentrated research in the direction of laser beam precise focusing. With a new era of 3D direct production of the objects from the powder, there have been problems related to mathematical and practical tools for the creation of uniform and disperse laser beams in the form of circles or even squares. Optical tools such as laser beam expanders are already installed in industrial SLM machines and are efficient for producing large objects such as hip implants and turbine blades with a dimensional length up to 35 cm. The modern focal shaper is known for its many practical solutions in laser manufacturing, but it still is not used in the industrial production of machines for selective laser melting and sintering.

The scheme of the developed setup is presented in Figure 6. The described profiles were experimentally achieved on the developed experimental setup (Figure 7). The distance between the  $f$ -Theta lens and the powder layer was calculated and was equal to 20 mm. At this distance, a donut laser beam profile was detected (Figure 7d). With the variation of this distance, a Gauss profile (Figure 7a) and large and small flat-top profiles were detected (Figure 7b,c). Further experiments were conducted with Gaussian, small flat-top and donut laser profiles. The achieved flat-top profiles do not look representative on 3D diagrams (Figure 7b,c) as it is difficult to obtain ones closer to the ideal cylindrical form mathematically and practically. The presented diagrams were registered at first approach on the experimental setup, and profiles close to those presented in Figure 4 was used for processing.



(a)



(b)

Figure 6. The principal scheme of the experimental setup: (a) optical and (b) mechanical parts.

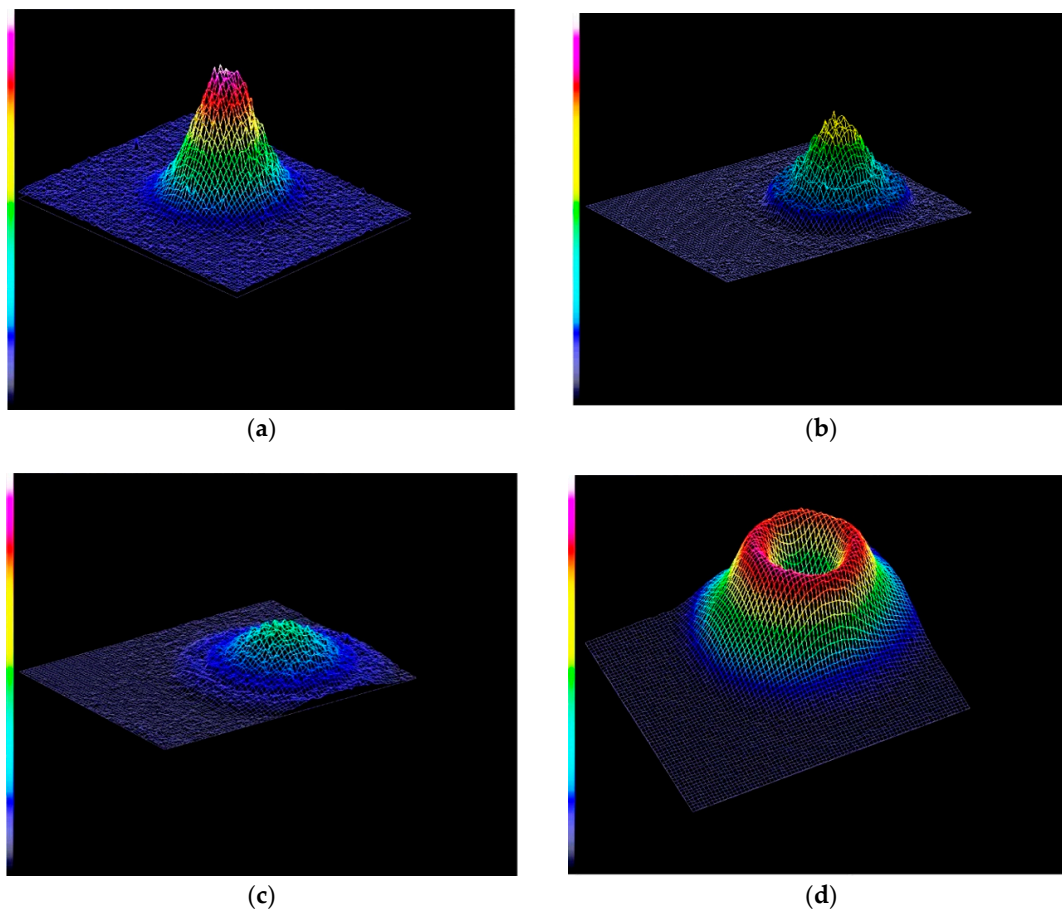


**Figure 7.** 3D images of the obtained laser beam profiles detected by the CCD camera of the optical monitoring system: (a) Gaussian laser beam  $TEM_{00}$  mode, the effective diameter of the spot  $D_{eff} = 111 \mu\text{m}$ ; (b) small flat top TFT =  $TEM_{00} + TEM_{01}^*$  mode, effective diameter of the spot  $D_{eff} = 260 \mu\text{m}$ ; (c) large flat top; (d) donut laser beam  $TEM_{01}^*$  mode; the effective diameter of the spot  $D_{eff} = 347 \mu\text{m}$ .

### 3.2.2. Formation of Single Tracks and its Characterization

Single tracks were produced with variations in the main factors, the laser beam power and scanning speed, to make precise the process gaps for further research into laser beam profiles. The laser beam power  $P$  varied from 10 to 173 W (the actual maximum value of the power) with increments of 10 W; the scanning speed  $V$  varied from 5 to 80 mm/s with increments of 10 mm/s.

During the experiments, there were two process gaps unveiled for each of the laser beam profiles (Table 2).

**Table 2.** Process parameters for CoCrMo powder with variation of laser beam profiles.

Laser Beam Profiles	Effective Diameter $D_{eff}^1$ (mm)	Group of SLM Parameters	Range of Values for Laser Power $P$ (W)	Range of Values for Scanning Speed $V_s$ (m/s)
Gaussian $TEM_{00}$	0.109	GAP I	30 ÷ 70	0.02 ÷ 0.05
		GAP II	130 ÷ 150	0.05 ÷ 0.07
flat top TFT = $TEM_{00} + TEM_{01}^*$	0.200	GAP I	50 ÷ 70	0.005 ÷ 0.03
		GAP II	130 ÷ 170	0.04 ÷ 0.08
donut $TEM_{01}^* = TEM_{01} + TEM_{10}$	0.300	GAP I	50 ÷ 70	0.01 ÷ 0.03
		GAP II	150 ÷ 173	0.05 ÷ 0.1

<sup>1</sup> Effective diameter  $D_{eff}$  was controlled by CCD camera.

The process gaps for each of the laser beam profiles showed a tendency to broaden with an increase in the effective diameter  $D_{eff}$ . The trend of enlargement was so clear that it is possible to guess that the higher borders of the discovered process windows were limited by the technological limits of the equipment (the laser beam source and the scanning head).

It was decided to compare the obtained results of optical microscopy for the tracks with the similar energetic contribution  $E$  ( $J \cdot m^{-2}$ ), which was calculated as follows:

$$E = \frac{P}{D_{eff} \cdot V_s}. \quad (5)$$

This approach may be simplified, but it allows for evaluating the results received with a similar energetic contribution for different diameters of the laser spot. Like this, the impact of the laser diameter is of secondary importance, while the impact of energy distribution is the priority.

Then the tracks, which were produced with an energetic contribution in the range between  $1.17 \times 10^7$  and  $1.70 \times 10^7 J \cdot m^{-2}$ , showed a different picture of the single-track formation (Figure 8). For the tracks obtained in the first process gap with the flat-top and donut laser profiles (Figure 8b,c), the relative depth of the track as a ratio of its depth versus the height of the track is not sufficient for the formation of the strong metallurgical contact between the layers [81,82]. The results obtained in the second process gap (Figure 8d–f) give a more acceptable picture of the formation, with higher values of the SLM factors. The tracks were consistent and regular, which may be sufficient and satisfactory for the creation of solid metallurgical contact with the previous layers [83–85].

The general view of the tracks is presented in Figure 9. The tracks have a mostly regular character. Figure 9e demonstrates the presence of the dynamic influence of the convective flows during the consecutive formation of the molten pools, which can be explained by the Peclet number related to the transport phenomena in a continuum [79,81]: at small values of the Peclet number, molecular thermal conductivity prevails, and at large values, convective heat transfer predominates.

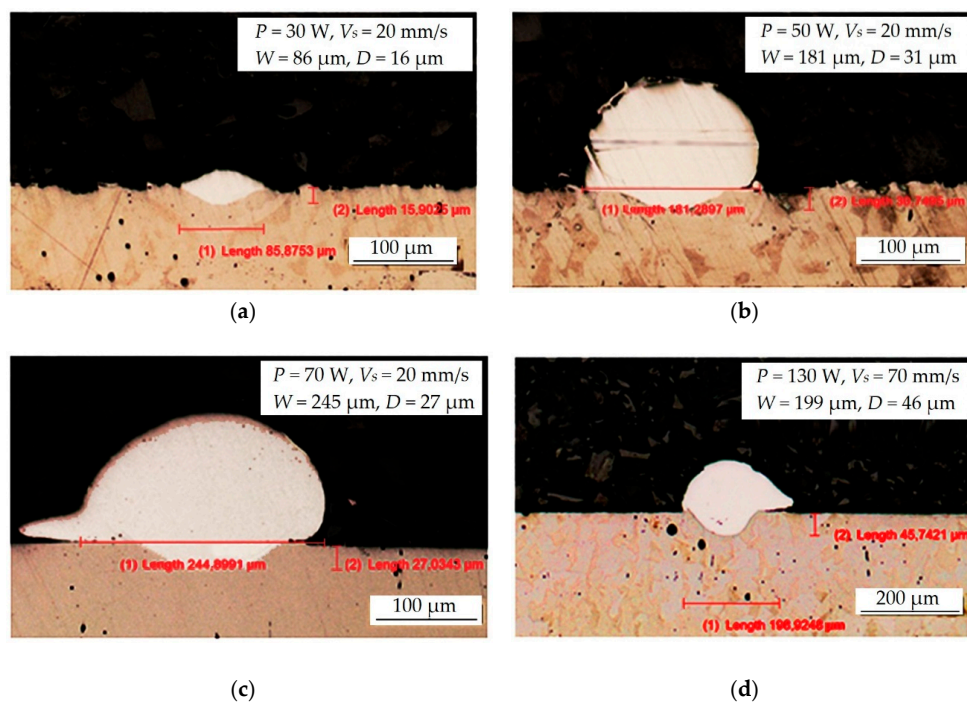
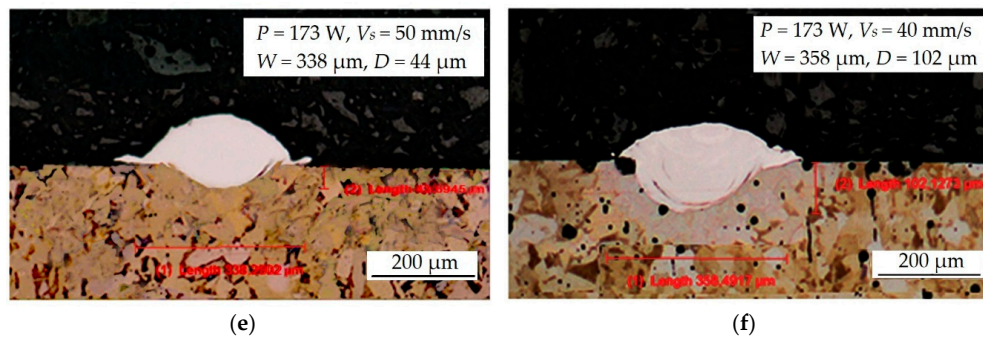
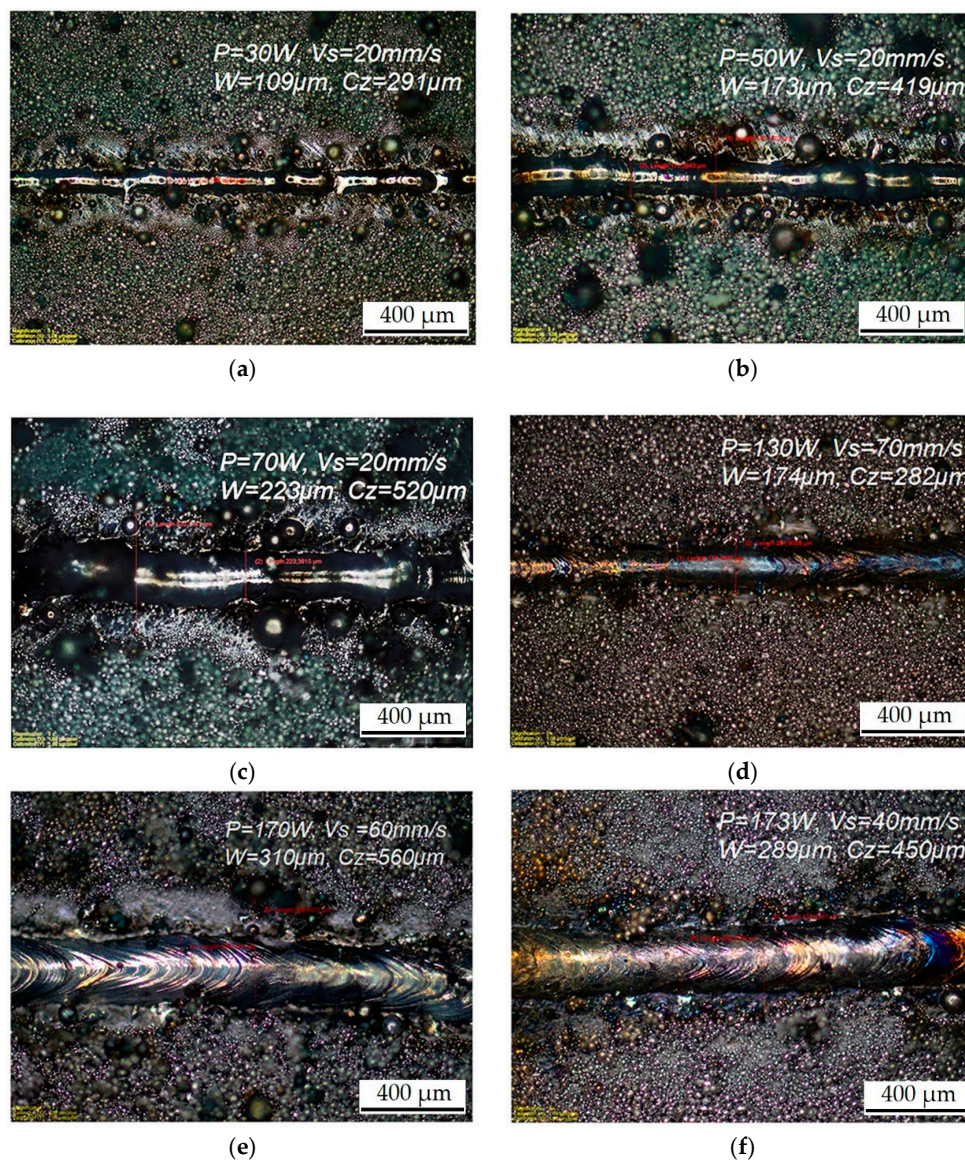


Figure 8. Cont.



**Figure 8.** Optical microscopy of the single track cross sections: (a) Gaussian in the first process gap; (b) flat top in the first process gap; (c) donut in the first process gap; (d) Gaussian in the second process gap; (e) flat top in the second process gap; (f) donut in the second process gap.  $W$  is the track width;  $D$  is the depth.



**Figure 9.** General view of the single tracks: (a) Gaussian in the first process gap; (b) flat top in the first process gap; (c) donut in the first process gap; (d) Gaussian in the second process gap; (e) flat top in the second process gap; (f) donut in the second process gap.  $W$  is the track width;  $C_z$  is the optically measured width of a heat-affected zone.

### 3.2.3. Analyses of Geometric Characteristics of the Tracks

The dependence of the track width on the laser power and scanning speed is presented in Table 3. The values in the cells are colored in grades between red and white following its values, where red is for its maximum value and white for an absence of metallurgical contact or experimental data due to an absence of practical interest in this field of research. The character of the graphs for different laser profiles does not show any noticeable changes with effective diameter increase. The values of width are close to or noticeably less than those for Gauss beam for flat-top tracks with laser power more than 100 W. At the same time, the effective diameter of the flat-top laser spot is approximately twice the effective diameter of the Gaussian laser spot. That confirms the better efficiency of energy absorption for the flat-top profile and can be recommended for improving the accuracy of objects produced with a laser power of more than 100 W.

**Table 3.** Average measured values of single-track width  $W$  ( $\mu\text{m}$ ) on process parameters for CoCrMo (the values are colored in grades of red for comparative evaluation of single-track width, where red is for the maximum value and white is for an absence of metallurgical contact or experimental data).

Laser Power $P$ , W	Scanning Speed $V_s$ , m/s									
	0.005	0.01	0.02	0.03	0.04	0.05	0.06	0.07	0.08	0.1
<b>Gauss</b>										
10	0 <sup>1</sup>	0	0	0	0	– <sup>2</sup>	–	–	–	–
30	0	0	109	94	86	90	–	–	–	–
50	0	200	141	164	133	119	115	102	0	0
70	238	257	200	185	188	0	0	0	0	136
100	326	312	287	238	250	0	0	187	0	0
130	345	344	315	263	363	236	220	178	0	0
150	404	372	309	335	301	225	287	198	251	209
170	415	393	335	0	405	0	310	269	252	182
173	474	401	408	338	346	332	297	246	323	279
<b>Flat-top</b>										
10	0	0	–	–	–	–	–	–	–	–
30	134	110	105	86	0	0	–	–	–	–
50	200	173	169	165	149	135	119	100	100	107
70	241	214	212	200	190	140	157	152	0	–
100	258	271	263	255	281	0	192	170	157	164
130	322	300	264	268	239	233	0	243	155	0
150	452	365	419	405	332	259	257	256	256	0
170	414	373	402	293	322	253	324	277	234	0
173	462	397	408	346	324	245	258	226	229	204
<b>Donut</b>										
10	0	0	–	–	–	–	–	–	–	–
30	0	0	0	0	–	–	–	–	–	–
50	213	186	182	0	0	0	0	0	0	–
70	224	237	232	230	186	174	0	148	0	0
100	238	235	232	237	219	238	201	201	197	176
130	308	403	296	235	346	258	239	234	0	0
150	406	398	304	337	232	350	211	207	190	204
170	384	287	265	347	253	237	254	210	205	215
173	473	418	462	269	321	347	342	372	259	235

<sup>1</sup> an absence of metallurgical contact or no track formed during processing; <sup>2</sup> an absence of experimental data.

Figure 10 shows the different character of the dependencies between the control SLM factors and measured track depth for different laser beam profiles. The dependencies presented in the form of 3D fields show that the character of the changes becomes smoother with a shift in the laser profile from Gaussian to donut. The first technological gap reduces from Gauss to donut; at the same time,

the second technological gap grows from accident results to a stable field of parameters (marked blue arrows). The maximum values of depth for each profile are shown in Table 4.

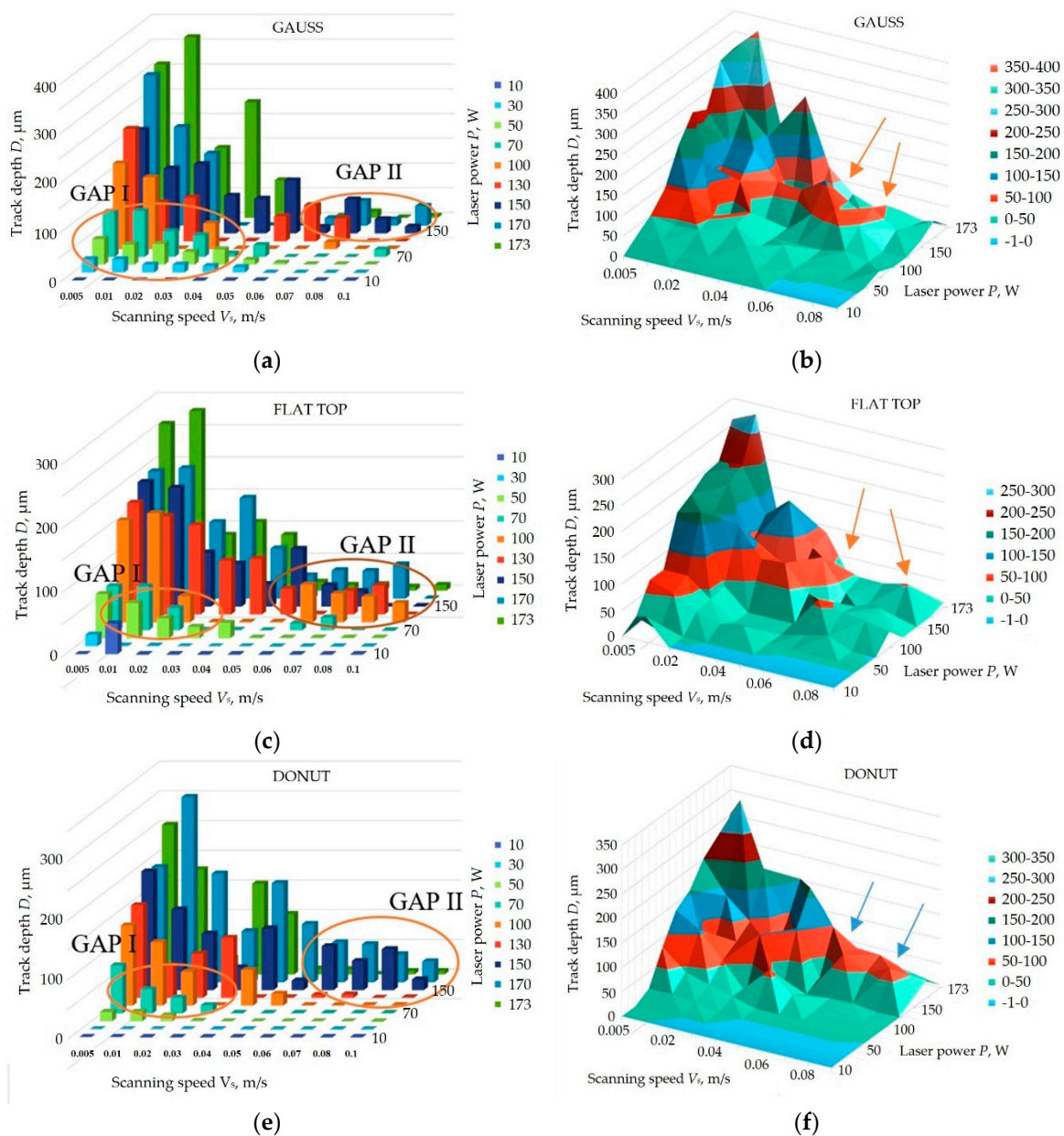


**Figure 10.** Dependence of single track depth  $D$  ( $\mu\text{m}$ ) on process parameters for CoCrMo powder: (a) bar graph for Gauss; (b) 3D graph for Gauss; (c) bar graph for flat top; (d) 3D graph for flat top; (e) bar graph for donut; (f) 3D graph for donut; an absence of metallurgical contact or not formed track during processing is marked as “0”.

**Table 4.** The maximum values of the depth for each profile during SLM production of single tracks from CoCrMo powder with the height of the layer  $\sim 80 \mu\text{m}$ .

Laser Beam Profiles	Max Depth of the Track ( $\mu\text{m}$ )	Range of Values for Laser Power $P$ (W)	Range of Values for Scanning Speed $V_s$ (m/s)
Gauss	365	173	0.01
Flat top	280	173	0.01
donut	312	170	0.01

The common picture of depth values showed the oscillating character of the change with the growth of the scanning speed from 0.005 m/s to 0.1 m/s. For the flat-top profile, the graphs acquire a correlated character despite non-periodic steps between the values of laser power (10, 70, 100, 150, 170, 173). For the donut profile, the graphs also acquire a correlated character but with doubled periodic behavior for the scanning speed and non-periodic steps between the values of laser power (70, 100, 150, 170).

The higher values of the SLM factors: for the flat top  $P = 100$  and  $170$  W,  $V_s = 0.06 \div 0.08$  m/s; for the donut  $P = 150 \div 170$  W,  $V_s = 0.06 \div 0.08$  m/s creates the stable process gaps. The sufficient values of the depths for the formation of the constant metallurgical contact were  $49.5 \pm 6.5 \mu\text{m}$  for the flat-top profile and  $58.5 \pm 10.5 \mu\text{m}$  for the donut profile.

Figure 11 presents optically measured absolute values of the heat-affected zone (HAZ, powder-free zone). The values of the relative heat-affected zone (Figure 12) were obtained by the next formula:

$$C_{z,r} = C_{z,a} - W, \quad (6)$$

where  $C_{z,r}$  is the relative value of the heat-affected zone,  $\mu\text{m}$ ; and  $C_{z,a}$  is the absolute measured value of the heat-affected zone,  $\mu\text{m}$ .

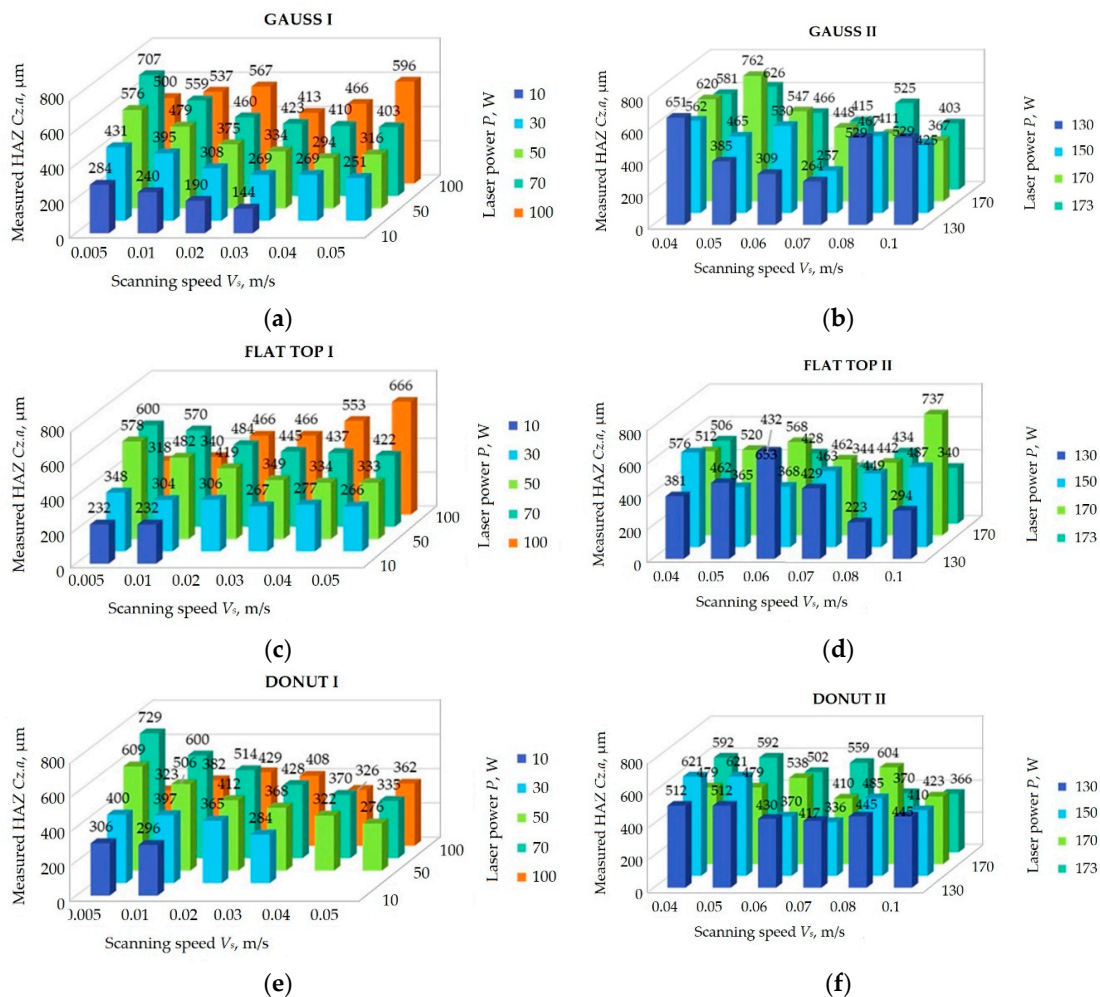


**Figure 11.** Dependence of heat-affected zone width of single tracks on process parameters for CoCrMo powder: (a) for technological gap I of Gauss; (b) for technological gap II of Gauss; (c) for technological gap I of flat top; (d) for technological gap II of flat top; (e) for technological gap I of donut; (f) for technological gap II of donut.

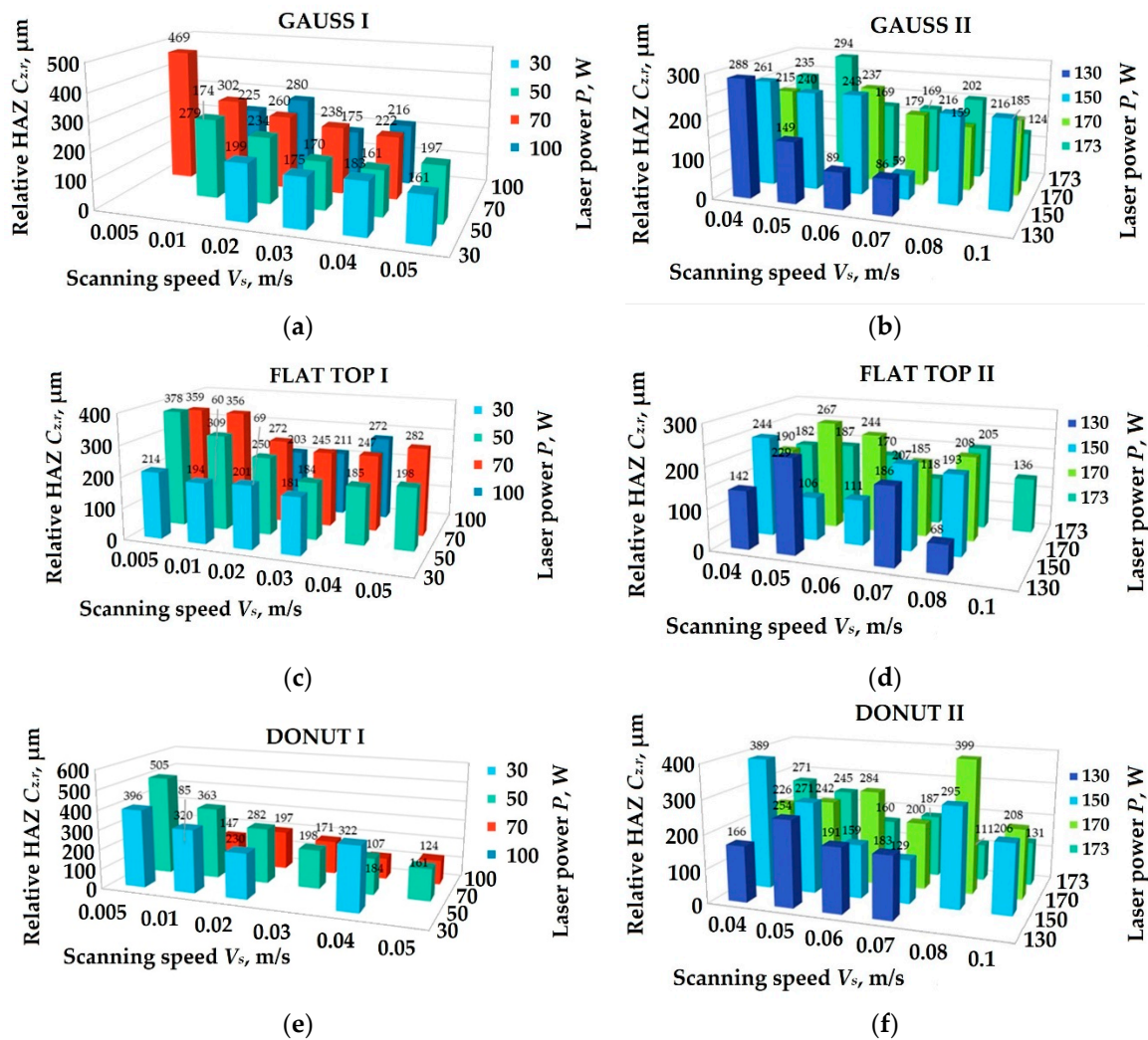


**Figure 12.** Dependence of relative heat-affected zone width of single tracks on process parameters for CoCrMo powder: (a) technological gap I of Gauss; (b) technological gap II of Gauss; (c) technological gap I of flat top; (d) technological gap II of flat top; (e) for technological gap I of donut; (f) technological gap II of donut.

The optically measured absolute values of the heat-affected zone have their lowest values for the flat-top (from 230 to 680  $\mu\text{m}$ ) and donut profiles (from 240 to 730  $\mu\text{m}$ ), which is preferable for SLM processing as it can solve the problem of a lack of powder during formation close to tracks.

The average values of HAZ for each value of laser power are presented in Table 5. The average values of relative HAZ for each value of laser power are presented in Table 6.

**Table 5.** The average values of heat-affected zone (HAZ)  $C_{z,a}$  ( $\mu\text{m}$ ) during SLM production of single tracks from CoCrMo powder with the height of the layer  $\sim 80 \mu\text{m}$ .

Laser Beam Profiles	Effective Diameter $D_{eff}$ ( $\mu\text{m}$ )	Laser Power $P$ (W)								
		10	30	50	70	100	130	150	170	173
		Scanning Speed $V_s$ (m/s)								
		0.005 ÷ 0.05						0.04 ÷ 0.1		
Gauss	109	214.5	320.5	395.7	493.7	513.2	444.5	451	525.8	502.7
flat top	200	232	294.7	415.8	493	468.2	407	451.3	540	414
donut	300	301	361.5	415.5	496	371.7	460	473.8	488	496.8

**Table 6.** The average values of relative HAZ  $C_{z,r}$  ( $\mu\text{m}$ ) during SLM production of single tracks from CoCrMo powder with the height of the layer  $\sim 80 \mu\text{m}$ .

Laser Beam Profiles	Effective Diameter $D_{eff}$ ( $\mu\text{m}$ )	Laser Power $P$ (W)									
		10 <sup>1</sup>	30 <sup>1</sup>	50	70	100	130	150	170	173	
		Scanning speed $V_s$ (m/s)									
		0.005 ÷ 0.05					0.04 ÷ 0.1				
Gauss	109	-	179.5	208.2	298.2	214	153	197.2	195	198.8	
flat top	200	-	197.5	250.7	293.5	163	156.3	172.2	218.8	166.3	
donut	300	-	-	269.3	282.2	138.5	198.5	241.5	259.8	184.2	

<sup>1</sup> The data for laser power 10 W and 30 W for donut profile are not provided due to the absence of metallurgical contact and absence of the formed track, which looks as a sequence of consolidated drops.

The most significant values of the heat-affected zone were obtained with the Gaussian profile (from 190 to 760  $\mu\text{m}$ ). The character of the graphs changes with the increase in laser power: At low values of laser power, the graphs have almost linear behavior; for large values of laser power, the graphs have a wavelike character. The better results of the absolute values of the heat-affected zone for the higher laser power (more than 150 W) is shown the flat-top and the donut profiles.

The range of values of the relative heat-affected zone is similar to each of the laser profiles. Meanwhile, the character of the data distribution tends to the increase of the dispersion of the values of the relative heat-affected zone width. It should be noted that the period of the wavelike graphs for the high values of the laser power has a tendency to double with the change of the laser profile from Gaussian to donut.

## 4. Discussion

### 4.1. Industrial SLM Equipment with Higher Laser Power

Nowadays, most modern SLM equipment with the maximum available laser power of about 400–1000 W uses the Gaussian laser beam profile modified by an expander. The role of the expander is to make the laser power density distribution more or less uniform on the spot—in other words, to redistribute the amount of energy at the laser spot on the treated surface (variance  $\sigma^2$ ). The authors propose going further and changing the mathematical function of laser power density distribution in the laser beam as technology practice meets problems related to the loss of quality of the parts with the direct augmentation of SLM parameters [18]. Most works on SLM equipment now are related to medical and dental applications, which demands a higher quality of production according to the individual models. Then the operational power does not exceed 30 W. For the production of large parts with a length of more than 150 mm, such as hip-bone implants, there is an opportunity to use higher laser power (up to 100 W), but with additional post-mechanical machining and polishing to achieve the required roughness and accuracy of the product. These experimental and practical data are supported by the results of video monitoring by the High-Speed Sync (HSS) camera presented in Figure 13, which shows the excess of energy in the molten pool in the form of granule emission at laser power 32 W and a low-temperature plasma cloud at 50 W. In both the cases it influences on the quality of the building object as a loss of material through granule emission and laser ablation, theoretically up to 5–15% of the powder layer thickness, if we do not take into account the thermal shrinkage of the material.

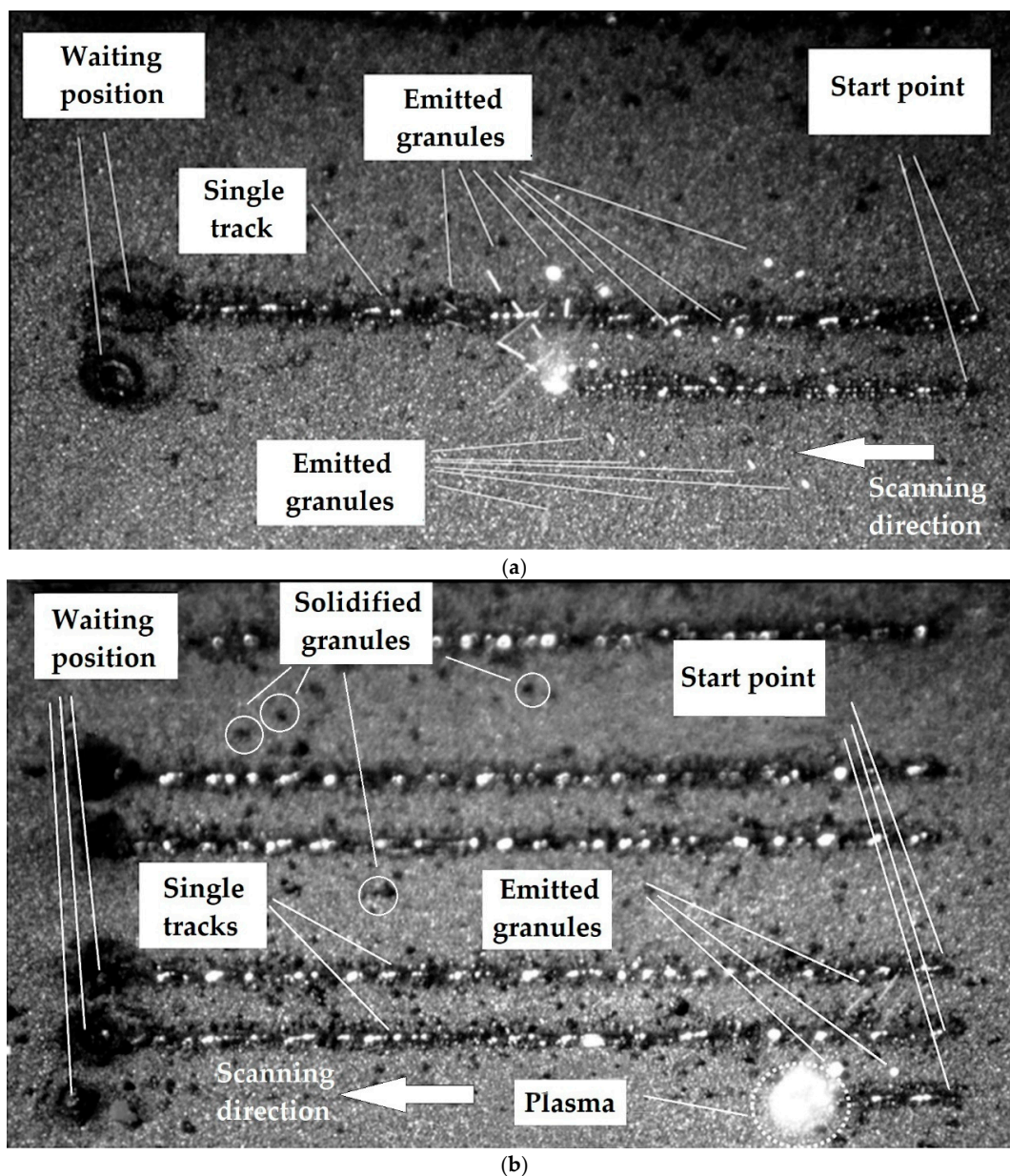


**Figure 13.** The result of video monitoring of SLM processing of CoCrMo powder (granule diameter  $d < 50 \mu\text{m}$ ) by high-speed camera with 810 nm filter: (a) SLM parameters: nominal laser power  $P = 32 \text{ W}$ , scanning speed  $V = 15 \text{ mm/s}$ , thickness of the layer  $h = \sim 80 \mu\text{m}$ ; (b) SLM parameters: nominal laser power  $P = 50 \text{ W}$ , scanning speed  $V = 15 \text{ mm/s}$ , thickness of powder layer  $h = \sim 80 \mu\text{m}$ .

#### 4.2. Discussion on Results of Video Monitoring

The preliminary results of video monitoring of single-track SLM processing (Figure 13) showed an excess of energy in the molten pool, which influences on the quality of track deposition and their geometric characterization [86].

The energy of the laser beam reaching the surface of the powder carries radiation pressure and radiation heat, which partly absorbed by the surface of the powder and partly reflected into the environment [87]. The simple Gaussian profile of the laser beam creates overheating in the center of the molten pool and consequently large temperature gradients between the center and its periphery. When the center of the molten pool receives an excess of heat, it provokes evaporation of the melted material, and creates sparks and granule emission (Figure 13a) for a nominal value of laser power even in the working chambers of industrial machines [88–90]. It should be noted that, for higher values of

laser power, the excess of energy leads to the formation of a plasma cloud [91], which accompanies the process (Figure 13b). At the same time, the periphery does not receive essential heat for starting the granules' melting process [92], which leads to the presence of nonmelted granules, which dragged into the convective flows of the liquid material in the molten pool. When some of the non-melted granules with convective flow reach the center of the molten pool, they are emitted into the atmosphere due to the thermal impact in the center of the molten pool. Preheating of the substrate can partially solve this problem, but it does not change the overall picture. Another set of these granules continues in the convective flow up to the moment of solidification, and then stays on the surface of the solidified surface of the molten pool (Figure 14) [93,94].

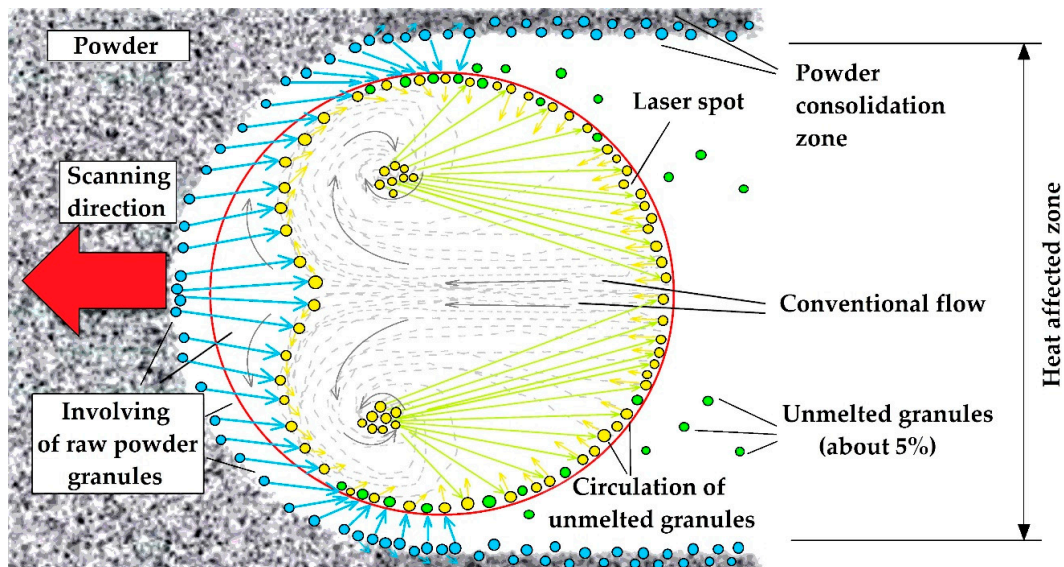


**Figure 14.** Analytical model of the convective flows and involvement of the raw powder into the melting process of the molten pool during selective laser melting.

#### 4.3. Achievability of the Alternative Laser Profiles

Classical density distribution related to the Gaussian function does not uniformly distribute the energy in the laser spot. There is an excess of energy closer to the center of the molten pool and a lack of energy at its periphery. The purpose of this work is to achieve uniform laser power density distribution by optical modulation of the laser beam. Theoretically, the flat-top or top-hat density distribution is preferable. At the same time, the TFT mode is hardly achievable mathematically or practically. However, it is possible to achieve a function with a uniform peak of energy in the middle. At the same time, obtaining inverse Gaussian mode  $TEM_{01}^*$  is quite a simple task. The theoretically absorbed energy with the distribution of the energy in the form of a donut function is more uniform than Gaussian and flat-top ones [18]. However, the effect during experiments with introduced dynamics due to the constant movement of the laser beam is quietly unpredictable and needs research.

#### 4.4. Influence of Laser Density Distribution on Geometry of the Tracks

Figure 9 shows that the widths of tracks for donut profile obtained in the field of factors with laser power less than 100 W have values close to or noticeably less than those for Gaussian profiles. At the same time, the effective diameter is three times less than the effective diameter of the Gaussian spot. This means that the donut profile can be suitable for the precise production of objects with laser power less than 100 W without the formation of a knife-like molten pool or too deep penetration into the substrate and its consequent interaction with subsequent layers, and reduces other negative consequences of the energy excess in the molten pool. Meanwhile, with values of laser power more than 100 W, the donut profile showed its ineffectiveness and a high rate of instability due to dynamic

convective and diffusive flows related to features of heat and mass transfer in double-diffusive convection. This shows the potential field of the application as flat-top and donut coincide with a domain of the Gaussian profile use because of the possibility of obtaining more or less the same or even more precise values for the widths of tracks.

It should be noted that the flat-top beam provides a broader field of process parameters for more uniform formation of the molten pool (Figure 10c,d), which is preferable for SLM processing of powder thickness less than  $80\ \mu\text{m}$  (Figure 10b,d,f, blue field of values). This can be seen even better in Figure 15, where for the broad field of the depth values are presented only tracks with the depth of less than  $60 \pm 5\ \mu\text{m}$ . With the thickness of the powder layer more than  $80\ \mu\text{m}$ , the donut laser beam profile can be recommended (Figure 10e,f, the red field of values) as it has a zone of “guaranteed” results.

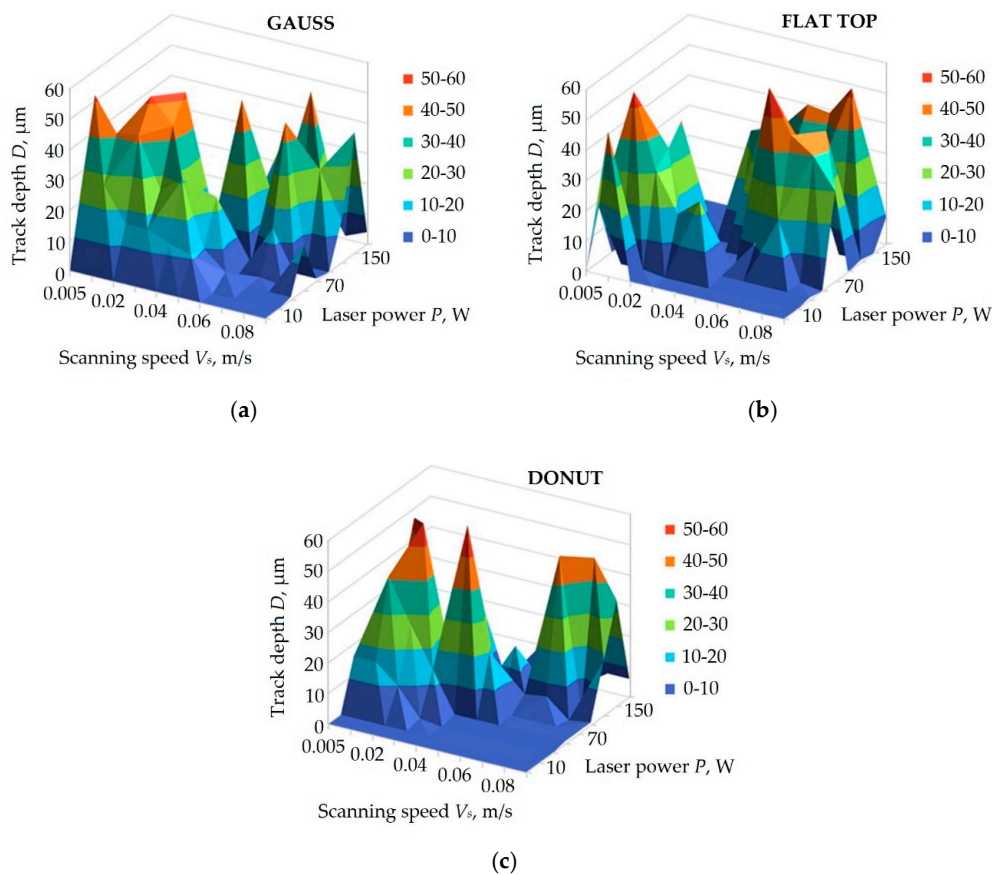


**Figure 15.** Dependence of the track depth on SLM parameters for CoCrMo powder for values less than  $60 \pm 5\ \mu\text{m}$ : (a) Gauss; (b) flat top; (c) donut.

The character of value depth distribution in the first technological gap (I) becomes irregular if, in the picture in Figure 10a,b, there can be seen regular dependencies for lower values of laser power; furthermore, it changes for flat top (Figure 10c,d) and becomes irregular towards donut (Figure 10e,f). The opposite tendency is noticed for the second technological gap.

It should be noted that the optimal value of track depth might be from one-third to two-thirds of layer thickness. For the thickness of powder layer  $\sim 80\ \mu\text{m}$ , the thickness should be in the range  $20 \pm 60\ \mu\text{m}$  to provide better metallurgical contact between the layers and at the same time exclude the involvement of the previous layers in the remelting process to ensure better metallurgical and chemical homogeneity. As is seen from the graph, the flat top provides a more complete technological field for homogenous and uniform track formation (Figure 10c,d). It is possible that the complete potential of the donut profile was not detected during the experiments due to the technological limitations of the equipment used (Figure 10e,f); this is a field for further research.

If we take as a criterion for stable track formation the ratio of depth to width of the track as 1:5, based on practical experience of working with SLM technology [18,83], it can be seen that the donut profile probably has the best prospects for further research (with laser power up to 1 kW and scanning speed up to 0.5 m/s). It shows high proportional stability at a laser power more than 130 W and scanning speed of more than 0.05 m/s. At the same time, the flat-top profile provides comparable stability for tracks in the first technological gap with laser power more than 70 W and scanning speed up to 0.05 m/s.

The graphs in Figure 11 for flat-top and donut laser profiles have a more regular character of HAZ values for the second technological gap than for the Gaussian beam (Figure 11b,d,f). It can be seen that the dispersion of values is quite intensive for laser power more than 100 W for Gaussian mode. At the same time, the values for laser power less than 100 W for the Gaussian mode show a regular and predictable character (Figure 11a). Its regularity increases with changes from Gaussian to donut mode. The absolute value of HAZ shows its decrease, with changes of mode for a few combinations of technological parameters, despite an increase in the value of effective diameter.

The lines of trends for average absolute and relative values of HAZ depending on effective diameter are presented in Figure 16. It shows that the redistribution of energy, despite a doubling or tripling of laser spot effective diameter, positively influences the formation of the track and keeps the absolute value of the HAZ close to the value for the Gaussian beam. At the same time, the relative value of HAZ has a decreased tendency for mean values of laser power and a moderately increased tendency for its higher values.

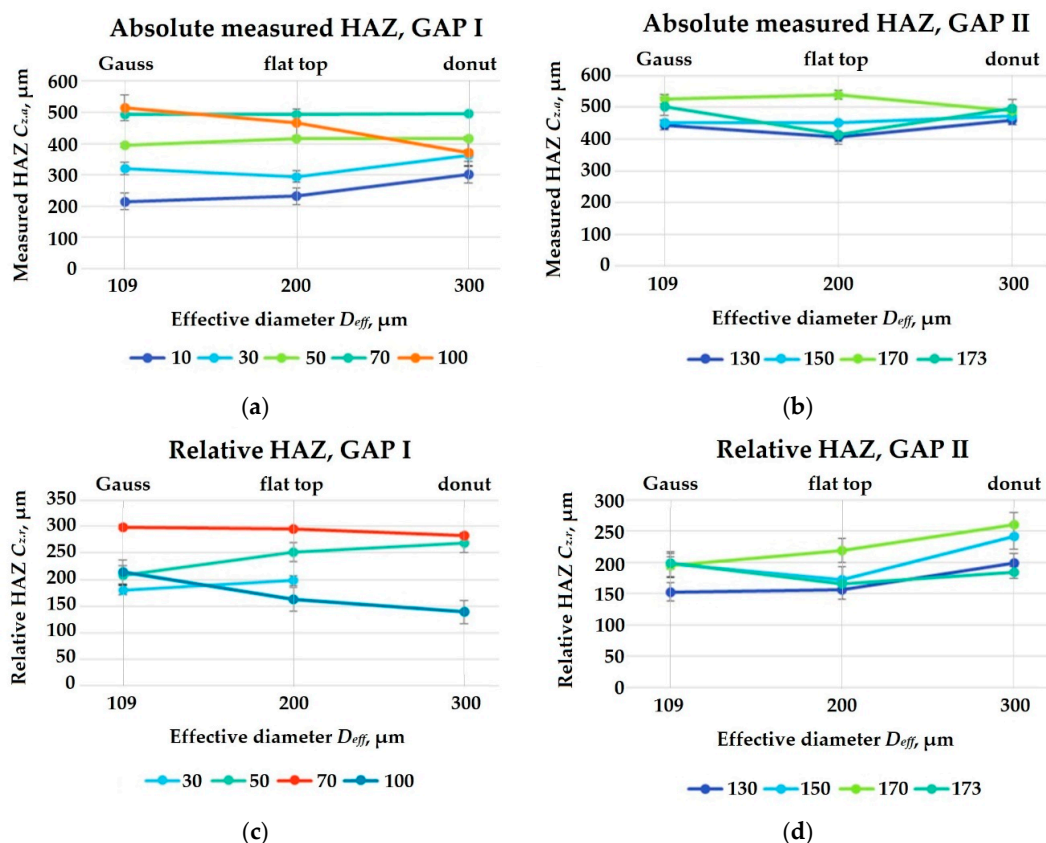


**Figure 16.** Dependence of average values of heat-affected zone (HAZ) on effective diameter for different values of laser power: (a) absolute value of HAZ for I technological gap for  $V_s = 0.005 \div 0.05$  m/s; (b) absolute value of HAZ for II technological gap for  $V_s = 0.04 \div 0.1$  m/s; (c) relative value of HAZ for I technological gap  $V_s = 0.005 \div 0.05$  m/s; (d) relative value of HAZ for II technological gap  $V_s = 0.04 \div 0.1$  m/s.

## 5. Conclusions

The experiments showed that power density distribution has an influence on the stability of processing when there is a gradual increase in the scanning speed and power of the laser source. All the theoretical laser beam modes were supported mathematically and obtained experimentally on the developed experimental setup. The results of modulation were verified by single track formation and the production of 3D objects from a CoCrMo alloy. The stability of processing was controlled optically; high-speed video recording provided data on the track-by-track sintering of the objects.

The application of the flat-top laser beam provided similar geometric parameters of the tracks, with a 14% augmentation of values for scanning speed and laser power in comparison with the Gaussian profile, which theoretically can allow for producing complex 3D objects with 14% higher efficiency. The same was achieved for the donut laser beam, but the general augmentation of the effectiveness may be about 43%. At the same time, the application of the donut profile gives such a bright, dynamic picture in the processing zone that higher values of the scanning speed may not provide the required quality for the obtained object layers.

It should be noted that the technical limitations of the used scanning head and laser source did not allow us to extend the experiments to the range of laser power 200–1000 W and do not unveil the full potential of the donut laser beam application, but it may have critical importance for the future of SLM technology.

The developed system of video monitoring is suitable for online control of the processing, which may have importance for the production of large-scale 3D objects or high-resolution objects. During the experiments, an advanced technique for reduction porosity of the samples was developed and applied. The obtained results can be extended to other techniques of laser additive manufacturing such as laser cladding, selective laser sintering of polymers or alloys reinforced by ceramics, and other laser-based 3D-printing techniques using liquid precursors as well as powders.

## 6. Patents

1. Smurov, I.Y.; Grigoriev, S.N.; Yadroitsev, I.A.; Okunkova, A.A.; Vladimirov, Yu. G. A Method of Manufacturing Products from Composite Powdered Materials; RU 2491152C1, 2013.08.27.
2. Kozochkin, M.P.; Okunkova, A.A.; Podrabinnik, P.A.; Peretyagin, P.Yu.; Safronov, V.A.; Khmyrov, R.S. Device for Laser Processing of Powder Materials; RU163795U1, 2016.08.10.

**Author Contributions:** Conceptualization, A.S.M. and A.A.O.; Methodology, A.S.M. and M.M.S.; Software, S.V.F.; Validation, S.V.F.; Formal Analysis, S.V.F.; Investigation, A.A.O.; Resources, M.M.S.; Data Curation, M.M.S.; Writing—Original Draft Preparation, A.A.O.; Writing—Review & Editing, A.A.O.; Visualization, S.V.F.; Supervision, A.S.M.; Project Administration, M.M.S.; Funding Acquisition, A.S.M.

**Funding:** This research was funded by the Ministry of Education and Science of Russian Federation, grant number no. 9.7889.2017/8.9.

**Acknowledgments:** The research was done at the Laboratories of the Department of High-Efficiency Machining Technologies of MSTU Stankin.

**Conflicts of Interest:** The authors declare no conflicts of interest.

## References

1. Zhang, K.; Mao, Z.; Fu, G.; Zhang, D.Z.; Liu, C.; Li, Z.H. A feasible method of support slimming based on the different thresholds of polar angles in selective laser melting. *Mater. Des.* **2018**, *157*, 501–511. [[CrossRef](#)]
2. Konstantinou, I.; Vosniakos, G.-C. Rough-cut fast numerical investigation of temperature fields in selective laser sintering/melting. *Int. J. Adv. Manuf. Technol.* **2018**, *99*, 29–36. [[CrossRef](#)]
3. Zavala-Arredondo, M.; Ali, H.; Groom, K.M.; Mumtaz, K. Investigating the melt pool properties and thermal effects of multi-laser diode area melting. *Int. J. Adv. Manuf. Technol.* **2018**, *97*, 1383–1396. [[CrossRef](#)]

4. AlMangour, B.; Grzesiak, D.; Cheng, J.; Ertas, Y. Thermal behavior of the molten pool, microstructural evolution, and tribological performance during selective laser melting of TiC/316L stainless steel nanocomposites: Experimental and simulation methods. *J. Mater. Process. Technol.* **2018**, *257*, 288–301. [[CrossRef](#)]
5. Salman, O.O.; Funk, A.; Waske, A.; Eckert, J.; Scudino, S. Additive Manufacturing of a 316L Steel Matrix Composite Reinforced with CeO<sub>2</sub> Particles: Process Optimization by Adjusting the Laser Scanning Speed. *Technologies* **2018**, *6*, 25. [[CrossRef](#)]
6. Song, W.; Wu, Y.; Gao, Y.; Chen, T.; Zheng, W.; Fang, H.; Song, L.; Yuan, X. Flexibly adjustable depth-of-focus photoacoustic microscopy with spatial light modulation. *Appl. Phys. Lett.* **2018**, *113*, 163502. [[CrossRef](#)]
7. Carluccio, D.; Birmingham, M.J.; Zhang, Y.; StJohn, D.H.; Yang, K.; Rometsch, P.A.; Wu, X.; Dargusch, M.S. Grain refinement of laser remelted Al-7Si and 6061 aluminium alloys with Tibor (R) and scandium additions. *J. Manuf. Process.* **2018**, *35*, 715–720. [[CrossRef](#)]
8. Nguyen, Q.B.; Zhu, Z.; Chua, B.W.; Zhou, W.; Wei, J.; Nai, S.M.L. Development of WC-Inconel composites using selective laser melting. *Arch. Civ. Mech. Eng.* **2018**, *18*, 1410–1420. [[CrossRef](#)]
9. Kang, N.; Ma, W.; Heraud, L.; El Mansori, M.; Li, F.; Liu, M.; Liao, H. Selective laser melting of tungsten carbide reinforced maraging steel composite. *Addit. Manuf.* **2018**, *22*, 104–110. [[CrossRef](#)]
10. Tan, C.; Zhou, K.; Ma, W.; Attard, B.; Zhang, P.; Kuang, T. Selective laser melting of high-performance pure tungsten: Parameter design, densification behavior and mechanical properties. *Sci. Technol. Adv. Mater.* **2018**, *19*, 370–380. [[CrossRef](#)]
11. Ivekovic, A.; Omidvari, N.; Vrancken, B.; Lietaert, K.; Thijs, L.; Vanmeensel, K.; Vleugels, J.; Kruth, J.-P. Selective laser melting of tungsten and tungsten alloys. *Int. J. Refract. Met. Hard Mater.* **2018**, *72*, 27–32. [[CrossRef](#)]
12. Enneti, R.K.; Morgan, R.; Atre, S.V. Effect of process parameters on the Selective Laser Melting (SLM) of tungsten. *Int. J. Refract. Met. Hard Mater.* **2018**, *71*, 315–319. [[CrossRef](#)]
13. Uhlmann, E.; Bergmann, A.; Bolz, R.; Gridin, W. Application of additive manufactured tungsten carbide tool electrodes in EDM. *Proc. CIRP* **2018**, *68*, 86–90. [[CrossRef](#)]
14. Banas, A.; Engay, E.; Bunea, A.-I.; Daedalus Separa, S.; Glückstad, J. Three-dimensional light sculpting using a geometric analysis. *Opt. Commun.* **2019**, *431*, 210–215. [[CrossRef](#)]
15. Bartolomeu, F.; Costa, M.M.; Gomes, J.R.; Alves, N.; Abreu, C.S.; Silva, F.S.; Miranda, G. Implant surface design for improved implant stability—A study on Ti6Al4V dense and cellular structures produced by Selective Laser Melting. *Tribol. Int.* **2019**, *129*, 272–282. [[CrossRef](#)]
16. Yang, L.; Yan, C.; Han, C.; Chen, P.; Yang, S.; Shi, Y. Mechanical response of a triply periodic minimal surface cellular structures manufactured by selective laser melting. *Int. J. Mech. Sci.* **2018**, *148*, 149–157. [[CrossRef](#)]
17. Wang, X.W.; Ho, J.Y.; Leong, K.C.; Wong, T.N. Condensation heat transfer and pressure drop characteristics of R-134a in horizontal smooth tubes and enhanced tubes fabricated by selective laser melting. *Int. J. Heat Mass Transf.* **2018**, *126*, 949–962. [[CrossRef](#)]
18. Gusarov, A.V.; Grigoriev, S.N.; Volosova, M.A.; Melnik, Y.A.; Laskin, A.; Kotoban, D.V.; Okunkova, A.A. On productivity of laser additive manufacturing. *J. Mater. Process. Technol.* **2018**, *261*, 213–232. [[CrossRef](#)]
19. Wei, M.; Chen, S.; Xi, L.; Liang, J.; Liu, C. Selective laser melting of 24CrNiMo steel for brake disc: Fabrication efficiency, microstructure evolution, and properties. *Opt. Laser Technol.* **2018**, *107*, 99–109. [[CrossRef](#)]
20. Wessels, H.; Weissenfels, C.; Wriggers, P. Metal particle fusion analysis for additive manufacturing using the stabilized optimal transportation meshfree method. *Comput. Methods Appl. Mech. Eng.* **2018**, *339*, 91–114. [[CrossRef](#)]
21. Aqilah, D.N.; Sayuti, A.K.M.; Farazila, Y.; Suleiman, D.; Amirah, M.; Izzati, W. Effects of Process Parameters on the Surface Roughness of Stainless Steel 316L Parts Produced by Selective Laser Melting. *J. Test. Eval.* **2018**, *46*, 1673–1683. [[CrossRef](#)]
22. Wen, S.; Dong, A.; Lu, Y.; Zhu, G.; Shu, D.; Sun, B. Finite Element Simulation of the Temperature Field and Residual Stress in GH536 Superalloy Treated by Selective Laser Melting. *Acta Metall. Sin.* **2018**, *54*, 393–403.
23. Anilli, M.; Demir, A.G.; Previtali, B. Additive manufacturing of laser cutting nozzles by SLM: Processing, finishing and functional characterization. *Rapid Prototyp. J.* **2018**, *24*, 562–583. [[CrossRef](#)]

24. Buchbinder, D.; Schleifenbaum, H.; Heidrich, S.; Meiners, W.; Bültmann, J. High Power Selective Laser Melting (HP SLM) of Aluminum Parts. *Phys. Procedia* **2011**, *12*, 271–278. [[CrossRef](#)]
25. Kumar, S.; Czekanski, A. Optimization of parameters for SLS of WC-Co. *Rapid Prototyp. J.* **2017**, *23*, 1202–1211. [[CrossRef](#)]
26. Kimura, T.; Nakamoto, T. Thermal and Mechanical Properties of Commercial-Purity Aluminum Fabricated Using Selective Laser Melting. *Mater. Trans.* **2017**, *58*, 799–805. [[CrossRef](#)]
27. Alfaify, A.Y.; Hughes, J.; Ridgway, K. Critical evaluation of the pulsed selective laser melting process when fabricating Ti64 parts using a range of particle size distributions. *Addit. Manuf.* **2018**, *19*, 197–204. [[CrossRef](#)]
28. Raus, A.A.; Wahab, M.S.; Ibrahim, M.; Kamarudin, K.; Aqeel, A.; Shamsudin, S. Mechanical and Physical Properties of AlSi10Mg Processed through Selective Laser Melting. *AIP Conf. Proc.* **2017**, *1831*, 020027.
29. Buchbinder, D.; Meiners, W.; Wissenbach, K. Selective laser melting of aluminum die-cast alloy-Correlations between process parameters, solidification conditions, and resulting mechanical properties. *J. Laser Appl.* **2015**, *27*, S29205. [[CrossRef](#)]
30. Yuan, P.; Gu, D. Molten pool behaviour and its physical mechanism during selective laser melting of TiC/AlSi10Mg nanocomposites: Simulation and experiments. *J. Phys. D Appl. Phys.* **2015**, *48*, 035303. [[CrossRef](#)]
31. Vrána, R.; Červinek, O.; Maňas, P.; Koutný, D.; Paloušek, D. Dynamic Loading of Lattice Structure Made by Selective Laser Melting-Numerical Model with Substitution of Geometrical Imperfections. *Materials* **2018**, *11*, 2129. [[CrossRef](#)] [[PubMed](#)]
32. Patel, R.; Hirsch, M.; Dryburgh, P.; Pieris, D.; Achamfuo-Yeboah, S.; Smith, R.J.; Light, R.A.; Sharples, S.D.; Clare, A.T.; Clark, M. Imaging Material Texture of As-Deposited Selective Laser Melted Parts Using Spatially Resolved Acoustic Spectroscopy. *Appl. Sci.* **2018**, *8*, 1991. [[CrossRef](#)]
33. Weißmann, V.; Boss, C.; Schulze, C.; Hansmann, H.; Bader, R. Experimental Characterization of the Primary Stability of Acetabular Press-Fit Cups with Open-Porous Load-Bearing Structures on the Surface Layer. *Metals* **2018**, *8*, 839. [[CrossRef](#)]
34. Siddique, S.; Awd, M.; Wiegold, T.; Klinge, S.; Walther, F. Simulation of Cyclic Deformation Behavior of Selective Laser Melted and Hybrid-Manufactured Aluminum Alloys Using the Phase-Field Method. *Appl. Sci.* **2018**, *8*, 1948. [[CrossRef](#)]
35. Hartunian, P.; Eshraghi, M. Effect of Build Orientation on the Microstructure and Mechanical Properties of Selective Laser-Melted Ti-6Al-4V Alloy. *J. Manuf. Mater. Process.* **2018**, *2*, 69. [[CrossRef](#)]
36. Okunkova, A.; Peretyagin, P.; Vladimirov, Y.; Volosova, M.; Torrecillas, R.; Fedorov, S.V. Laser-beam modulation to improve efficiency of selecting laser melting for metal powders. *Proc. SPIE* **2014**, *9135*, 913524.
37. Kotoban, D.; Grigoriev, S.; Okunkova, A.; Sova, A. Influence of a shape of single track on deposition efficiency of 316L stainless steel powder in cold spray. *Surf. Coat. Technol.* **2017**, *309*, 951–958. [[CrossRef](#)]
38. Isaev, A.; Grechishnikov, V.; Pivkin, P.; Kozochkin, M.; Ilyuhin, Y.; Vorotnikov, A. Machining of thin-walled parts produced by additive manufacturing technologies. *Procedia CIRP* **2016**, *41*, 1023–1026.
39. Isaev, A.V.; Kozochkin, M.P. Use of a Measurement Information System to Increase the Precision with which Thin-Walled Parts are Machined on Numerically Controlled Milling Machines. *Meas. Tech.* **2014**, *56*, 1155–1161. [[CrossRef](#)]
40. Kozochkin, M.P.; Porvatov, A.N.; Sabirov, F.S. The fitting of technological equipment with data-measuring systems. *Meas. Tech.* **2012**, *55*, 530–534. [[CrossRef](#)]
41. Metel, A.S.; Grigoriev, S.N.; Melnik, Y.A.; Prudnikov, V.V. Glow discharge with electrostatic confinement of electrons in a chamber bombarded by fast electrons. *Plasma Phys. Rep.* **2011**, *37*, 628–637. [[CrossRef](#)]
42. Kim, W.C.; Park, N.C. Effect of birefringence of lens material on polarization status and optical imaging characteristics. *Opt. Commun.* **2018**, *413*, 329–335.
43. Peng, C.; He, Y.; Wang, J. Optimization of pencil beam f-theta lens for high-accuracy metrology. *Opt. Eng.* **2018**, *57*, 015101. [[CrossRef](#)]
44. Grigoriev, S.N.; Kozochkin, M.P.; Sabirov, F.S.; Kutin, A. Diagnostic Systems as Basis for Technological Improvement. *Procedia CIRP* **2012**, *1*, 599–604. [[CrossRef](#)]
45. Kozochkin, M.P.; Porvatov, A.N.; Sabirov, F.S. Vibration Testing of Technological Processes in Automated Machining Equipment. *Meas. Tech.* **2014**, *56*, 1414–1420. [[CrossRef](#)]

46. Liu, Z.; Wu, J.; Zhang, Y.; Zhang, Y.X.; Tang, X.Y.; Yang, X.H.; Zhang, J.Z.; Yang, J.; Yuan, L.B. Optical trapping and axial shifting for strongly absorbing particle with single focused TEM00 Gaussian beam. *Appl. Phys. Lett.* **2018**, *113*, 091101. [[CrossRef](#)]
47. Bhebhe, N.; Rosales-Guzman, C.; Forbes, A. Classical and quantum analysis of propagation invariant vector flat-top beams. *Appl. Opt.* **2018**, *57*, 5451–5458. [[CrossRef](#)] [[PubMed](#)]
48. Olikier, V.; Doskolovich, L.L.; Bykov, D.A. Beam shaping with a plano-freeform lens pair. *Opt. Express* **2018**, *26*, 19406–19419. [[CrossRef](#)] [[PubMed](#)]
49. Naidoo, D.; Litvin, I.A.; Forbes, A. Brightness enhancement in a solid-state laser by mode transformation. *Optica* **2018**, *5*, 836–843. [[CrossRef](#)]
50. Kanzler, K.J. Transformation of a Gaussian laser beam to an Airy pattern for use in focal plane intensity shaping using diffractive optics. *Proc. SPIE* **2001**, *4443*, 58–66. [[CrossRef](#)]
51. Almeida, J.; Liang, D.; Vistas, C.R. A doughnut-shaped Nd: YAG solar laser beam. *Opt. Laser Technol.* **2018**, *106*, 1–6. [[CrossRef](#)]
52. Prashanth, K.G.; Scudino, S.; Chatterjee, R.P.; Salman, O.O.; Eckert, J. Additive Manufacturing: Reproducibility of Metallic Parts. *Technologies* **2017**, *5*, 8. [[CrossRef](#)]
53. Bassoli, E.; Denti, L. Assay of Secondary Anisotropy in Additively Manufactured Alloys for Dental Applications. *Materials* **2018**, *11*, 1831. [[CrossRef](#)] [[PubMed](#)]
54. Zhuang, Y.-X.; Zhang, X.-L.; Gu, X.-Y. Effect of Annealing on Microstructure and Mechanical Properties of Al<sub>0.5</sub>CoCrFeMo<sub>x</sub>Ni High-Entropy Alloys. *Entropy* **2018**, *20*, 812. [[CrossRef](#)]
55. Wang, J.-H.; Ren, J.; Liu, W.; Wu, X.-Y.; Gao, M.-X.; Bai, P.-K. Effect of Selective Laser Melting Process Parameters on Microstructure and Properties of Co-Cr Alloy. *Materials* **2018**, *11*, 1546. [[CrossRef](#)] [[PubMed](#)]
56. Harun, W.S.W.; Kamariah, M.S.I.N.; Muhamad, N.; Ghani, S.A.C.; Ahmad, F.; Mohamed, Z. A review of powder additive manufacturing processes for metallic biomaterials. *Powder Technol.* **2018**, *327*, 128–151. [[CrossRef](#)]
57. Bai, Y.; Fu, F.; Xiao, Z.; Zhang, M.; Wang, D.; Yang, Y.; Song, C. Progress in selective laser melting equipment, related biomedical metallic materials and applications. *J. Zhejiang Univ. Sci. A* **2018**, *19*, 122–136. [[CrossRef](#)]
58. Yang, Y.Z.; Ong, J.L.; Tian, J. Deposition of highly adhesive ZrO<sub>2</sub> coating on Ti and CoCrMo implant materials using plasma spraying. *Biomaterials* **2003**, *24*, 619–627. [[CrossRef](#)]
59. Kuzin, V.V.; Grigor'ev, S.N.; Volosova, M.A. Effect of a TiC Coating on the Stress-Strain State of a Plate of a High-Density Nitride Ceramic under Nonsteady Thermoelastic Conditions. *Refract. Ind. Ceram.* **2014**, *54*, 376–380. [[CrossRef](#)]
60. Volosova, M.A.; Grigor'ev, S.N.; Kuzin, V.V. Effect of Titanium Nitride Coating on Stress Structural Inhomogeneity in Oxide-Carbide Ceramic. Part 4. Action of Heat Flow. *Refract. Ind. Ceram.* **2015**, *56*, 91–96. [[CrossRef](#)]
61. Essa, K.; Sabouri, A.; Butt, H.; Basuny, F.H.; Ghazy, M.; El-Sayed, M.A. Laser additive manufacturing of 3D meshes for optical applications. *PLoS ONE* **2018**, *13*, e0192389. [[CrossRef](#)]
62. Nguyen, V.L.; Kim, E.-A.; Lee, S.-R.; Yun, J.; Choe, J.; Yang, D.-Y.; Lee, H.-S.; Lee, C.-W.; Yu, J.-H. Evaluation of Strain-Rate Sensitivity of Selective Laser Melted H13 Tool Steel Using Nanoindentation Tests. *Metals* **2018**, *8*, 589. [[CrossRef](#)]
63. Metel, A.; Bolbukov, V.; Volosova, M.; Grigoriev, S.; Melnik, Y. Source of metal atoms and fast gas molecules for coating deposition on complex shaped dielectric products. *Surf. Coat. Technol.* **2013**, *225*, 34–39. [[CrossRef](#)]
64. Metel, A.S. Ionization Effect in Cathode Layers on Glow-Discharge Characteristics with Oscillating Electrons. 1. Discharge with the Hollow-Cathode. *Zhurnal Tekh. Fiz.* **1985**, *55*, 1928–1934.
65. Metel, A.; Bolbukov, V.; Volosova, M.; Grigoriev, S.; Melnik, Y. Equipment for Deposition of Thin Metallic Films Bombarded by Fast Argon Atoms. *Instrum. Exp. Tech.* **2014**, *57*, 345–351. [[CrossRef](#)]
66. Chang, C.; Chen, X.; Chen, Z.; Lin, Z.; Li, X.; Pu, J. Experimental investigation on a nonuniformly correlated partially coherent laser. *Appl. Opt.* **2018**, *57*, 4381–4385. [[CrossRef](#)] [[PubMed](#)]
67. Gupta, D.K.; Tata, B.V.R.; Ravindran, T.R. A Technique to Calibrate Spatial Light Modulator for Varying Phase Response over its Spatial Regions. *AIP Conf. Proc.* **2018**, *1953*, 140112.
68. Bell, T.; Hasnaoui, A.; Ait-Ameur, K.; Ngcobo, S. Excitation of high-radial-order Laguerre-Gaussian modes in a solid-state laser using a lower-loss digitally controlled amplitude mask. *J. Opt.* **2017**, *19*, 105604. [[CrossRef](#)]

69. Wang, M.; Zong, L.; Mao, L.; Marquez, A.; Ye, Y.; Zhao, H.; Vaquero Caballero, F.J. LCoS SLM Study and Its Application in Wavelength Selective Switch. *Photonics* **2017**, *4*, 22. [[CrossRef](#)]
70. Wang, H.; Piestun, R. Dynamic 2D implementation of 3D diffractive optics. *Optica* **2018**, *5*, 1220–1228. [[CrossRef](#)]
71. Kang, N.; El Mansori, M.; Guittonneau, F.; Liao, H.; Fu, Y.; Aubry, E. Controllable mesostructure, magnetic properties of soft magnetic Fe-Ni-Si by using selective laser melting from nickel coated high silicon steel powder. *Appl. Surf. Sci.* **2018**, *455*, 736–741. [[CrossRef](#)]
72. Drexler, M.; Greiner, S.; Lexow, M.; Lanzl, L.; Wudy, K.; Drummer, D. Selective laser melting of polymers: Influence of powder coating on mechanical part properties. *J. Polym. Eng.* **2018**, *38*, 667–674. [[CrossRef](#)]
73. Papadakis, L.; Chantzis, D.; Salonitis, K. On the energy efficiency of pre-heating methods in SLM/SLS processes. *Int. J. Adv. Manuf. Technol.* **2018**, *95*, 1325–1338. [[CrossRef](#)]
74. Wang, X.; Kustov, S.; Van Humbeeck, J. A Short Review on the Microstructure, Transformation Behavior and Functional Properties of NiTi Shape Memory Alloys Fabricated by Selective Laser Melting. *Materials* **2018**, *11*, 1683. [[CrossRef](#)] [[PubMed](#)]
75. Kumar, V.; Dixit, U.S.; Zhang, J. Determination of thermal conductivity, absorptivity and heat transfer coefficient during laser-based manufacturing. *Measurement* **2019**, *131*, 319–328. [[CrossRef](#)]
76. Zhang, Z.; Huang, Y.; Kasinathan, A.R.; Imani Shahabad, S.; Ali, U.; Mahmoodkhani, Y.; Toyserkani, E. 3-Dimensional heat transfer modeling for laser powder-bed fusion additive manufacturing with volumetric heat sources based on varied thermal conductivity and absorptivity. *Opt. Laser Technol.* **2019**, *109*, 297–312. [[CrossRef](#)]
77. Yadroitsev, I.; Gusarov, A.; Yadroitsava, I.; Smurov, I. Single track formation in selective laser melting of metal powders. *J. Mater. Process. Technol.* **2010**, *210*, 1624–1631. [[CrossRef](#)]
78. Gusarov, A.V.; Gnedovets, A.G.; Smurov, I. Two-dimensional gas-dynamic model of laser ablation in an ambient gas. *Appl. Surf. Sci.* **2000**, *154*, 66–72. [[CrossRef](#)]
79. Gusarov, A.; Liegeois, F. Experimental study of a tunable fiber ring laser stability. *Opt. Commun.* **2004**, *234*, 391–397. [[CrossRef](#)]
80. Gusarov, A.V.; Smurov, I. Two-dimensional numerical modelling of radiation transfer in powder beds at selective laser melting. *Appl. Surf. Sci.* **2009**, *255*, 5595–5599. [[CrossRef](#)]
81. Sova, A.; Okunkova, A.; Grigoriev, S. Velocity of the Particles Accelerated by a Cold Spray Micronozzle: Experimental Measurements and Numerical Simulation. *J. Therm. Spray Technol.* **2013**, *22*, 75–80. [[CrossRef](#)]
82. Sobol', O.V.; Andreev, A.A.; Grigoriev, S.N.; Volosova, M.A.; Gorban, V.F. Vacuum-arc multilayer nanostructured TiN/Ti coatings: Structure, stress state, properties. *Met. Sci. Heat Treat.* **2012**, *54*, 28–33. [[CrossRef](#)]
83. Tarasova, T.V.; Nazarov, A.P.; Prokof'ev, M.V. Effect of the regimes of selective laser melting on the structure and physicomechanical properties of cobalt-base superalloys. *Phys. Met. Metallogr.* **2015**, *116*, 601–605. [[CrossRef](#)]
84. Grigor'ev, S.N.; Tarasova, T.V.; Gvozdeva, G.O.; Nowotny, S. Micro-Laser Facing of Al-Si System Alloys. *Met. Sci. Heat Treat.* **2013**, *55*, 242–246. [[CrossRef](#)]
85. Grigoriev, S.N.; Tarasova, T.V.; Gvozdeva, G.O.; Nowotny, S. Microcladding of hypereutectic Al-Si alloys: Technological aspects and structure features. *Int. J. Cast Met. Res.* **2014**, *27*, 357–361. [[CrossRef](#)]
86. Shi, X.; Ma, S.; Liu, C.; Wu, Q. Parameter optimization for Ti-47Al-2Cr-2Nb in selective laser melting based on geometric characteristics of single scan tracks. *Opt. Laser Technol.* **2017**, *90*, 71–79. [[CrossRef](#)]
87. Santos, L.M.S.; de Jesus, J.; Ferreira, J.M.; Costa, J.D.; Capela, C. Fracture Toughness of Hybrid Components with Selective Laser Melting 18Ni300 Steel Parts. *Appl. Sci.* **2018**, *8*, 1879. [[CrossRef](#)]
88. Fedorov, S.V.; Pavlov, M.D.; Okunkova, A.A. Effect of structural and phase transformations in alloyed subsurface layer of hard-alloy tools on their wear resistance during cutting of high-temperature alloys. *J. Frict. Wear* **2013**, *34*, 190–198. [[CrossRef](#)]
89. Sova, A.; Doubenskaia, M.; Grigoriev, S.; Okunkova, A.; Smurov, I. Parameters of the Gas-Powder Supersonic Jet in Cold Spraying Using a Mask. *J. Therm. Spray Technol.* **2013**, *22*, 551–556. [[CrossRef](#)]
90. Fousova, M.; Dvorsky, D.; Vronka, M.; Vojtech, D.; Lejcek, P. The Use of Selective Laser Melting to Increase the Performance of AlSi9Cu3Fe Alloy. *Materials* **2018**, *11*, 1918. [[CrossRef](#)]

91. Kovalev, O.B.; Yudin, P.V.; Zaitsev, A.V. Formation of a vortex flow at the laser cutting of sheet metal with low pressure of assisting gas. *J. Phys. D Appl. Phys.* **2008**, *41*, 155112. [[CrossRef](#)]
92. Kovaleva, I.O.; Kovalev, O.B. Simulation of the acceleration mechanism by light-propulsion for the powder particles at laser direct material deposition. *Opt. Laser Technol.* **2012**, *44*, 714–725. [[CrossRef](#)]
93. Kovalev, O.B.; Gurin, A.M. Multivortex convection of metal in molten pool with dispersed impurity induced by laser radiation. *Int. J. Heat Mass Transf.* **2014**, *68*, 269–277. [[CrossRef](#)]
94. Han, X.; Sawada, T.; Schille, C.; Schweizer, E.; Scheideler, L.; Geis-Gerstorfer, J.; Rupp, F.; Spintzyk, S. Comparative Analysis of Mechanical Properties and Metal-Ceramic Bond Strength of Co-Cr Dental Alloy Fabricated by Different Manufacturing Processes. *Materials* **2018**, *11*, 1801. [[CrossRef](#)] [[PubMed](#)]



© 2018 by the authors. Licensee MDPI, Basel, Switzerland. This article is an open access article distributed under the terms and conditions of the Creative Commons Attribution (CC BY) license (<http://creativecommons.org/licenses/by/4.0/>).